Orbits for the Impatient: A Bayesian Rejection Sampling Method for Quickly Fitting the Orbits of Long-Period Exoplanets

by

Sarah Blunt

A thesis submitted in partial fulfillment for the
degree of Bachelor of Science

in the
Dell'Antonio Group
Brown University Physics Department

May 2017

BROWN UNIVERSITY

Abstract

Dell'Antonio Group
Brown University Physics Department

Bachelor of Science

by Sarah Blunt

The orbits of directly-imaged exoplanets are often not well-constrained by data, resulting in impractical slow-downs or failures of traditional orbit-fitting algorithms. In this thesis, I describe a novel Bayesian rejection sampling algorithm designed to perform optimally in this regime, jointly developed by myself, Eric Nielsen, and several other collaborators. Our implementation of this method, Orbits for the Impatient (OFTI), converges up to several orders of magnitude faster than two implementations of the commonly-used family of Markov Chain Monte Carlo (MCMC) orbit-fitting methods in this regime. For example, in the case of β Pic b, OFTI fits 2.5 months of data in less than 0.1 minutes, while MCMC takes more than 15 hours to converge on the correct result. I demonstrate the accuracy of OFTI by comparing our results for several orbiting systems with those of various MCMC implementations, finding the output posteriors to be identical within shot noise. I also illustrate OFTI's computational efficiency through further MCMC comparisons and a detailed description of the algorithm itself.

Next, I describe several ways that OFTI has been applied within the astronomical community. By successfully predicting the future locations of directly imaged exoplanets, producing fits to tens of individual systems, and modeling the reduction of orbital parameter uncertainty for future space-based exoplanet detectors, OFTI is shown to be a valuable, practical astronomical tool. Finally, I discuss the scientific questions that OFTI enables us to explore.

Acknowledgements

Contents

For Allison Blunt, who birthed me, and bathed me, and changed my diapers, and clothed me, and raised me, and taught me, and never forgets to remind me.

Chapter 1

Introduction

Since the detection of the first extrasolar planet (exoplanet) in 1992, thousands of exoplanets have been discovered by several techniques, finally enabling astronomers to make statistical inferences about exoplanet populations. As the field of exoplanet science transitions from a focus of discovery to a focus on analysis, efficient statistical tools are becoming crucially important (e.g. [1]).

Direct imaging is a particularly valuable technique for studying exoplanets, since directly detecting the light emitted by an exoplanet enables spectral characterization (e.g. [38]). Several exoplanets have now been discovered and characterized using imaging technology, and government agencies such as NASA are heavily investing in long-term applications of this technology.

Direct imaging is sensitive to substellar objects (exoplanets and brown dwarfs) with large projected separations from their host objects ($\gtrsim 0.2$"; e.g. [37], [11]), corresponding to larger orbital semi-major axes and periods compared to those detected with radial velocity and transit methods [5]. Therefore, over timescales of months to years, direct imaging observations often probe only short fractions of these orbits. In these cases, constraints on orbital parameters can be used to perform a preliminary characterization of the orbit (e.g. [2], [49], [42], [55], [14], [67], [54]). Orbital parameter constraints can also lead to mass constraints on directly imaged substellar objects (e.g. [35], [18]), constraints on additional planets in the system [6], and information about the interactions between planets and circumstellar disks (e.g. [49], [42], [54]). In addition, orbit fitting can be used to constrain the future locations of exoplanets, notably to calculate the probability of a transit (e.g. [65]), or to determine an optimal cadence of observations to reduce uncertainty in orbital parameter distributions. For future direct imaging space missions such as the *Wide-Field Infrared Survey Telescope* (*WFIRST*; [60], [63]), it is

particularly important to quickly and accurately fit newly discovered exoplanet orbits in order to plan future observations efficiently.

Several orbital fitting methods are currently used in astronomy. The family of Bayesian Markov Chain Monte Carlo methods (MCMC) was introduced to the field of exoplanet orbit fitting by Ford (2004, 2006) and has been widely used (e.g. [49], [42], [17]). MCMC is designed to quickly locate and explore the most probable areas of parameter space for a particular set of data, and takes longer to converge as a parameter space becomes less constrained by data, as in the case of astrometry from a fraction of a long-period orbit. In addition, many types of MCMC algorithms can be inefficient at exploring parameter spaces if the corresponding χ^2 surface is complicated (e.g. [20]). Another commonly used tool for fitting orbits is the family of least-squares Monte Carlo (LSMC) methods [52], which uses a Levenberg-Marquardt minimization algorithm to locate the orbital fit with minimum χ^2 value for a set of astrometry. Once the minimum χ^2 orbit is discovered, this method then randomly varies the measured astrometry along Gaussian distributions defined by the observational errors. In cases where the parameter space is very unconstrained, this method often explores only the area closest to the minimum χ^2 orbit, leading to biases against areas of parameter space with lower likelihoods. For example, Chauvin et al. [10] found significantly different families of solutions when using LSMC than when using MCMC for the same orbital data for β Pic b. LSMC is therefore effective at finding the best-fit solution, but not well-suited to characterizing uncertainty by fully exploring the parameter space.

In this work, I present and discuss Orbits for the Impatient (OFTI), a Bayesian Monte Carlo rejection sampling method based on that described in Ghez et al. [26], and similar to methods described in Konopacky et al. [33] and Price-Whelan et al. [53]. OFTI is designed to quickly and accurately compute posterior probability distributions from astrometry covering a fraction of a long-period orbit. I describe how OFTI works and demonstrate its accuracy by comparing OFTI to two independent MCMC orbit-fitting methods. I then discuss situations where OFTI is most optimally used, and apply OFTI to several sets of astrometric measurements from the literature.

Chapter 2

Background

2.1 Direct Imaging

The success of orbit-fitting algorithms like OFTI depends on the accuracy of astrometric measurements derived from images of exoplanets. Obtaining direct images of exoplanets is a complicated task that requires advanced technology, both hardware and software. In addition, accurately measuring and modeling sources of systematic errors is essential for precision astrometry. In this section, I outline some of the important technologies that support exoplanet imaging.

2.1.1 Coronagraphy

Since the ratio of the intensity of even the brightest exoplanet to its primary star (contrast) is extremely small (10^{-4} - 10^{-6}), a necessary requirement of exoplanet imaging is suppressing the light from the primary object enough to reliably detect and characterize the light from the secondary object. This is accomplished using coronagraphs, optical systems within imaging instruments that attenuate the central starlight and suppress extraneous diffraction.

2.1.2 Adaptive Optics

High-contrast imaging requires that the phase errors effects of Earth's atmosphere be mitigated. To reduce phase errors, direct imaging instruments employ adaptive optics systems. An incoming distorted wavefront is fed into a wavefront sensor, which measures how it has been distorted by the atmosphere. Next, a computer uses the information from the wavefront sensor to calculate how to adjust a deformable mirror to correct for

the atmospheric distortion. Finally, the mirrors are deformed in real time, correcting the wavefronts on a timescale comparable to the time it takes the atmosphere to change significantly.

2.1.3 Integral Field Spectroscopy

Some advanced high-contrast imagers, such as the Gemini Planet Imager [37] (GPI) and SPHERE, make use of integral field spectrometers for imaging exoplanets. Once the light from an exoplanet has traveled through the coronagraph and adaptive optics systems of one of these instruments, it is detected by an integral field spectrometer (IFS), a device that produces a spectrum for each location on a spatial grid. The result is a datacube, a two-dimensional image with a third spectral dimension. GPI uses an array of spatially separated lenslets as its IFS. A two-dimensional wavefront passes through the lenslet array and a subsequent prism, and the spectra produced are projected onto a grid of pixels. Specialized data reduction pipelines are then used to turn the information detected by pixel array into datacubes (e.g. [51]).

2.2 Keplerian Orbit Parametrization

Keplerian orbits, or orbits described by classical two-body gravitational interactions, are parametrized by the following orbital elements (Fig 2.1):

1. Semi-major axis of the orbit ellipse (a)

2. Eccentricity (e)

3. Orbital period (P; related to the semi-major axis and the total system mass by Kepler's third law)

4. Epoch of periastron passage (T_0; time of exoplanet's closest approach to its host object)

5. Inclination angle (i)

6. Position angle of nodes (Ω)

7. Argument of periastron (ω)

a and e account for the two degrees of freedom in the shape of the orbital ellipse, while i, Ω, and ω (corresponding to the Euler angles of classical mechanics) orient the orbital
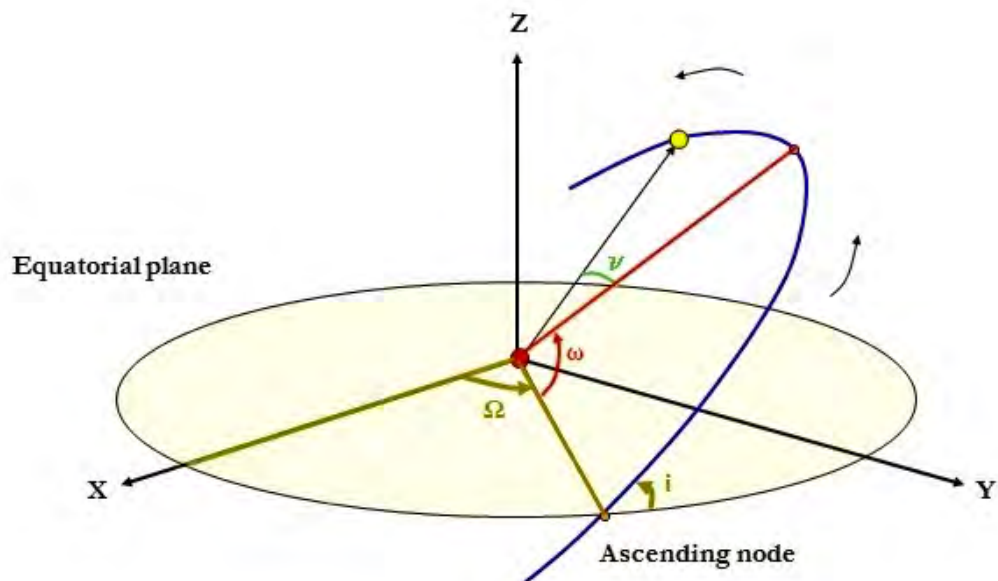
FIGURE 2.1: Orbit parametrization illustrating the three angular orbital parameters. The observer is located along the z-axis, while the reference direction ("North") is along the x-axis. Image credit: yoghaken.blogspot.com.

plane in space and give the location of periastron in that plane. The remaining two orbital elements (P and T_0) locate the exoplanet within its orbit at a given time. Together with the astronomical distance to the star, these elements completely characterize a Keplerian orbit viewed from Earth.

2.3   Orbit Fitting Overview

Orbit fitting is the process of converting data into a set of probability distributions describing families of possible orbits. In this thesis, I focus on orbit fitting to astrometric data, or data taken from direct images of exoplanets (Figure 2.2). Advanced image analysis algorithms (see, e.g. [65]) determine the precise projected location of an exoplanet relative to its primary companion and estimate the errors on these measurements. Together with the time at which the image was taken, or epoch, these location measurements compose one astrometric point. Several of these points, taken over time, are used as the input data for orbit fitting algorithms like OFTI.
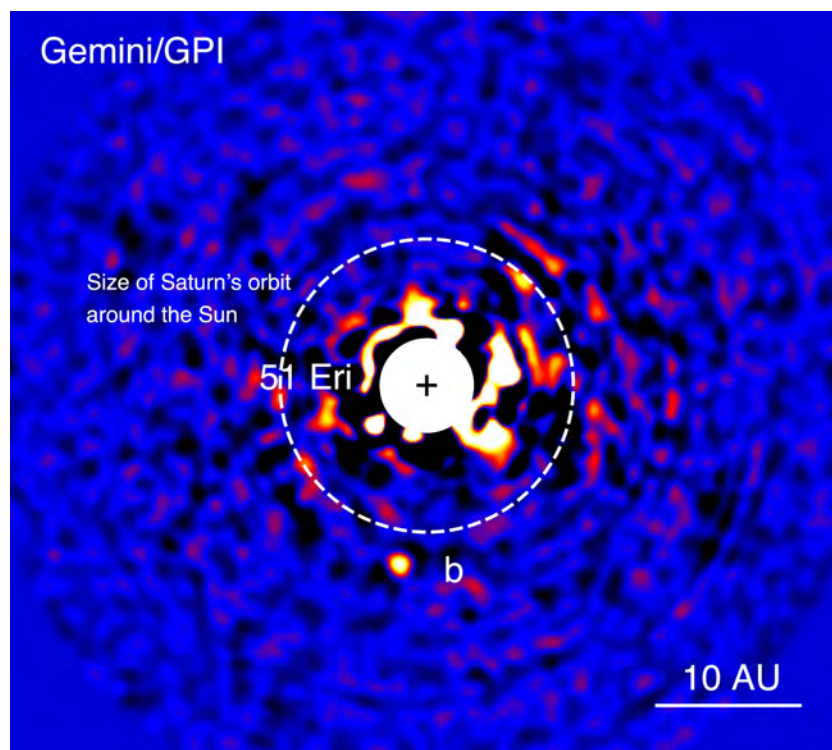
FIGURE 2.2: Direct image of the exoplanet 51 Eri b (after image processing) taken using the Gemini Planet Imager. The light from the star centered in this image has been physically blocked out using a coronagraph. Image credit: J. Rameau.

Chapter 3

The OFTI Algorithm

3.1 Method

OFTI, like other Bayesian methods, combines astrometric observations and uncertainties with prior probability density functions (PDFs) to produce posterior PDFs of orbital parameters. These orbital parameter posteriors allow us to better characterize systems, for example by predicting future motion or by directly comparing the orbital plane to the orbits of other objects in the system or the distribution of circumstellar material.

The basic OFTI algorithm consists of the following steps:

1. Monte Carlo Orbit Generation from Priors
2. Scale-and-Rotate
3. Rejection sampling

OFTI uses a modified Bayesian rejection sampling algorithm. Rejection sampling consists of generating random sets of parameters, calculating a probability for each value, and preferentially rejecting values with lower probabilities. For OFTI, the generated parameters are the orbital elements (a, P, e, i, Ω, ω, and T_0). For Bayesian rejection sampling algorithms such as OFTI, the candidate density functions used to generate these random parameters are prior probability distributions.

3.1.1 Monte Carlo Orbit Generation from Priors

OFTI begins by generating an initial set of seven random orbital parameters drawn from prior probability distributions. For the fits in this thesis, unless otherwise stated, we

used a linearly descending eccentricity prior with a slope of -2.18 for exoplanets, derived from the observed distribution of exoplanets detected by the radial velocity method [46]. The use of this prior assumes that long-period exoplanets follow the same eccentricity distribution as the planets detected by the radial velocity method. While the shape of the eccentricity prior directly affects the shape of the eccentricity posterior, as we would expect, the posteriors of other parameters are less affected when changing between a linearly descending and a uniform prior (see section 4.1). We assume a purely random orientation of the orbital plane, which translates into a $\sin(i)$ prior in inclination angle and uniform priors in the epoch of periastron passage and argument of periastron. That is, the inclination angle, position angle of nodes, and argument of periastron priors are purely geometric. OFTI initially generates orbits with $a = 1\,\mathrm{au}$ and $\Omega = 0\,^\circ$, but these values are altered in the following step. We note that OFTI can be easily run using different priors, making it useful for non-planetary systems and statistical tests.

3.1.2   Scale-and-Rotate

Once OFTI has generated an initial set of orbital parameters from the chosen priors, it performs a "scale-and-rotate" step in order to restrict the wide parameter space of all possible orbits. This increases the number of orbits accepted in the rejection sampling step. The generated semi-major axis and position angle of nodes are scaled and rotated, respectively, so that the new modified set of parameters describes an orbit that intersects a single astrometric data point. OFTI also takes the observational uncertainty of the data point used for the scale-and-rotate step into account. For each generated orbit, random offsets are introduced in separation (ρ) and position angle (θ) from Gaussian distributions with standard deviations equal to the astrometric errors at the scale-and-rotate epoch. These offsets are added to the measured astrometric values, and then the generated orbit is scaled-and-rotated to intersect the offset data point, rather than the measured data point. The scale-and-rotate step produces a uniform prior in Ω, and imposes a $\log(a)$ prior in semi-major axis. The posterior distributions OFTI produces are independent of the epoch chosen for this step, but the efficiency of the method is not. Some choices of the scale-and-rotate epoch result in a much higher fraction of considered orbits being accepted, and so the orbit is fit significantly faster. In order to take advantage of this change in efficiency, our implementation of OFTI performs an initial round of tests that pick out the scale-and-rotate epoch resulting in the largest acceptance rate of orbits, then uses this epoch every subsequent time this step is performed. The scale-and-rotate step differentiates OFTI from a true rejection sampling algorithm.

3.1.3   Rejection Sampling

Using the modified semi-major axis and position angle of nodes values, OFTI generates predicted ρ and θ values for all remaining epochs. OFTI then calculates the χ^2 probability for the predicted astrometry given the measured astrometry and uncertainties. This probability, assuming uncorrelated Gaussian errors, is given by: $p \propto e^{-\chi^2/2}$.

Finally, OFTI performs the rejection sampling step; it compares the generated probability to a number randomly chosen from a uniform distribution over the range (0,1). If the generated probability is greater than this random number, the generated set of orbital parameters is accepted.

This process is repeated until a desired number of generated orbits has been accepted (see Figure 3.1). As with MCMC, histograms of the accepted orbital parameters correspond to posterior PDFs of the orbital elements.

The OFTI implementation written by myself and my collaborators makes use of several computational and statistical techniques to speed up the basic algorithm described above:

- Our implementation uses vectorized array operations rather than iterative loops wherever possible. For example, instead of generating one set of random orbital parameters at a time, our program generates arrays containing 10,000 sets of parameters, and performs all subsequent operations on these arrays. Our program then iterates over this main loop, accepting and rejecting in batches of 10,000 generated orbits at a time. 10,000 is the empirically determined optimal number for our implementation.

- Our implementation of OFTI is written to run in parallel on multiple CPUs (our default is 10), speeding up runtime by a constant factor.

- Our implementation of OFTI is equipped with a statistical speedup that increases the fraction of orbits accepted per orbits tested. Due to measurement errors, the minimum χ^2 orbit typically has a χ^2 value greater than 0. OFTI makes use of this fact by calculating the minimum χ^2 value of all orbits tested during an initial run, then subtracting this minimum value from all future generated χ^2 values, rendering them more likely to be accepted in the method's rejection step. In rejection sampling, having a random variable whose range is much greater than the maximum probability doesn't change the distribution of parameters, but does result in more rejected trials.
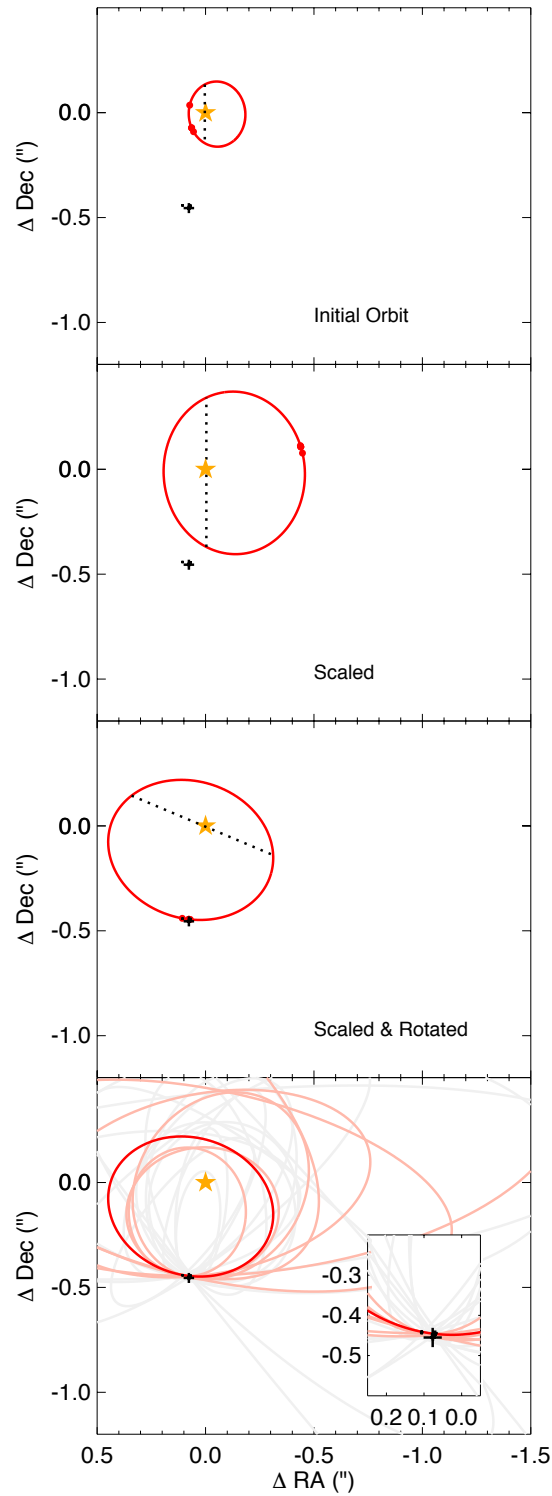
FIGURE 3.1: Visualization of the OFTI method. Known astrometry (in this figure, for 51 Eri b), is shown as black crosses. The yellow star at (0,0) shows the location of 51 Eri A. Top: an orbit with $a = 1\,\mathrm{au}$, $\Omega = 0\,^\circ$, and other orbital elements randomly drawn from appropriate priors is generated. Red dots along the orbit show the astrometric locations of 51 Eri b at the times of the observational epochs. The dotted line shows the line of nodes. Panels Two and Three: the scale-and-rotate step is performed. Bottom Panel: orbits accepted (light red) and rejected (gray) by the rejection sampling step of the OFTI algorithm. Inset: close up of bottom panel.

- Our implementation of OFTI also restricts the ranges of the input i and total mass priors based on initial results. After our implementation has accepted 100 orbits, it uses the maximum, minimum, and standard deviation of the array of accepted parameters to infer safe upper and lower limits to place on the relevant prior. This changes only the range of the relevant prior, not the shape of the prior. This speedup prevents our implementation of OFTI from wasting time generating orbits that have a negligible chance of being accepted.

3.2   Validation with MCMC

To illustrate that OFTI returns identical results to MCMC over short orbital arcs, I show a fit to the same orbit and priors with OFTI and two MCMC orbit-fitting routines: the Metropolis Hastings MCMC algorithm described in [49], and an Affine Invariant MCMC [22] orbit fitter from [37]. In Figure 3.2, I show the Metropolis Hastings MCMC and OFTI posterior PDFs calculated from astrometry of the system SDSS J105213.51+442255.7 AB (hereafter SDSS 1052; [16]) from 2005-2006. SDSS 1052 is a pair of brown dwarfs with period of approximately 9 years. We chose only a subset of the available astrometry of SDSS 1052 to illustrate the effect of fitting a short orbital arc. In addition, we assume a fixed system mass, and we use astrometry provided in Table 2 of [16]. The posterior distributions produced by OFTI and the Metropolis-Hastings MCMC are identical. OFTI was also validated using the relative astrometry of 51 Eri b, a directly imaged exoplanet discovered by the GPI Exoplanet Survey in 2015 ([38], [14]). In Figure 3.3, I plot the posterior distributions produced by all three methods, calculated from relative astrometry of 51 Eri b taken between 2014 December and 2015 September. As in the previous case, all three sets of posterior distributions produced by OFTI and the two MCMC implementations are identical.

An important difference between MCMC and OFTI involves the types of errors on the posteriors produced by the two methods. Because each step of OFTI is independent of previous steps, deviations from analytical posteriors have the form of uncorrelated noise, i.e. if our implementation of OFTI is run until 100 orbits are accepted, the output posteriors will not be biased, but simply noisy. As our implementation of OFTI is run until greater numbers of orbits are accepted, noise reduces by $\sqrt{N}$. MCMC steps, on the other hand, are not independent. Because the next MCMC step depends on the current location in parameter space, an un-converged MCMC run will result in biased, rather than noisy, posteriors. This is especially important in cases where MCMC has not been run long enough to achieve a satisfactory Gelman-Rubin (GR) statistic (a measure of convergence; [25]). In these cases, OFTI produces an unbiased result, while MCMC

does not. This situation is illustrated in Figure 3.4, showing the posteriors produced by a Metropolis-Hastings implementation of MCMC and our implementation of OFTI for all known astrometry of ROXs 42B b ([32], [12], [6]). After running for 30 hours on 10 CPUs, the MCMC posteriors are still un-converged, as can be seen by the lumpy shape of the Ω posterior. As a result, we see biases in the other posteriors. The GR statistics for each parameter were between 1.1 and 1.5 (an acceptable GR statistic is $\lesssim 1.01$, see e.g. [20]). Our implementation of OFTI produced this result in 134 minutes, more than an order of magnitude faster than MCMC.

To demonstrate the differences in the random errors incurred by OFTI and the systematic errors of MCMC, and to illustrate OFTI's computational speed for short orbital arcs, we calculated how the semi-major axis distributions generated by OFTI and MCMC changed as more sets of orbital elements were accepted for OFTI, and generated for MCMC. For both OFTI and MCMC, we calculate the median of the first n semi-major axes tested as a function of n, resulting in an array of medians for OFTI and an array of medians for MCMC. We then take the ratio of each number in these arrays to the median of the complete distribution of tested semi-major axes. Since MCMC and OFTI converge on the same distributions, the medians of both complete semi-major axis distributions are the same. As n approaches the total number of orbits tested, the partial distributions approach the complete distribution, and the ratios approach 1. We repeat this procedure for the lower and upper $1\,\sigma$ limits of the OFTI and MCMC semi-major axis distributions. These results are shown in Figure 3.5 for the orbit of 51 Eri b. Note that this represents the number of orbits tested, rather than number of orbits accepted, and so is directly proportional to computation time. After approximately 10^4 orbits are tested, the OFTI semi-major axis distribution (red line) converges on the final median semi-major axis (to within $5\,\%$), while the MCMC semi-major axis distribution (black line) suffers from systematic over- and under-estimates of the final semi-major axis value until more than 3 orders of magnitude more orbits have been tested. Similarly, OFTI converges on the appropriate $1\,\sigma$ upper and lower limits for the output semi-major axis distribution (to within $5\,\%$) after approximately 10^5 orbits are tested, while it takes MCMC 10^8 correlated steps in order to do the same.

OFTI is most efficient for astrometry covering smaller fractions of orbits, while MCMC achieves convergence faster for larger fractions of orbits. Figure 3.6 illustrates this difference by displaying the wallclock time per CPU needed for each method to achieve convergence using astrometry from β Pic b [42]. In order to compare the time for convergence by MCMC and OFTI, we define a proxy for convergence time: our distributions are said to be "converged" for a statistic of interest (e.g. a median, a $68\,\%$ confidence interval) when the statistic is within $1\,\%$ of the final value, where the final value is calculated from a distribution of 10^4 accepted orbits. From this analysis, we conclude
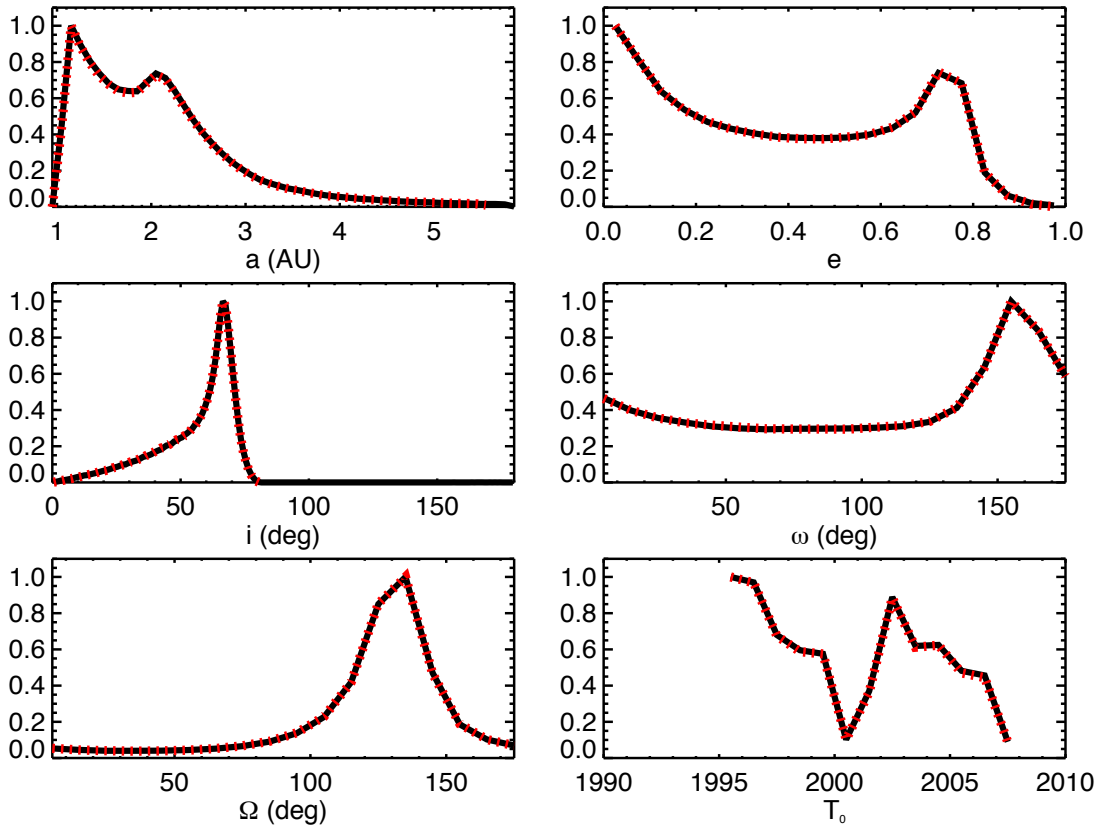
FIGURE 3.2: Normalized PDFs of the orbital parameters corresponding to orbits accepted by OFTI (red) and MCMC (black) for astrometry of the 9 year period binary brown dwarf SDSS 1052 from 2005-2006. The PDFs are identical, differing only by shot noise.

that OFTI is more efficient than MCMC for astrometry covering short orbital arcs, but becomes less efficient as more of the orbit is covered by astrometry.

For astrometry covering small fractions of a total orbit, OFTI can compute accurate future location predictions in much less time than MCMC. We illustrate this application in Figure 3.7, which shows probability distributions predicting the ρ, θ of 51 Eri b on 2015 September 15 from four earlier astrometric points taken over a timespan of less than 2 months [38]. Overplotted is the actual measured location of 51 Eri b. The predicted and observed medians for ρ are 0.455 ± 0.086 and 0.4547 ± 0.0057, and for θ are 170 ± 4 and 166.5 ± 0.6. This prediction analysis was made before the September 2015 astrometric data were obtained. 51 Eri A was unobservable between February and September of 2015. It took OFTI less than 5 minutes (running in parallel on ten 2.3 GHz AMD Opteron 6378 processors) to produce these predictions.
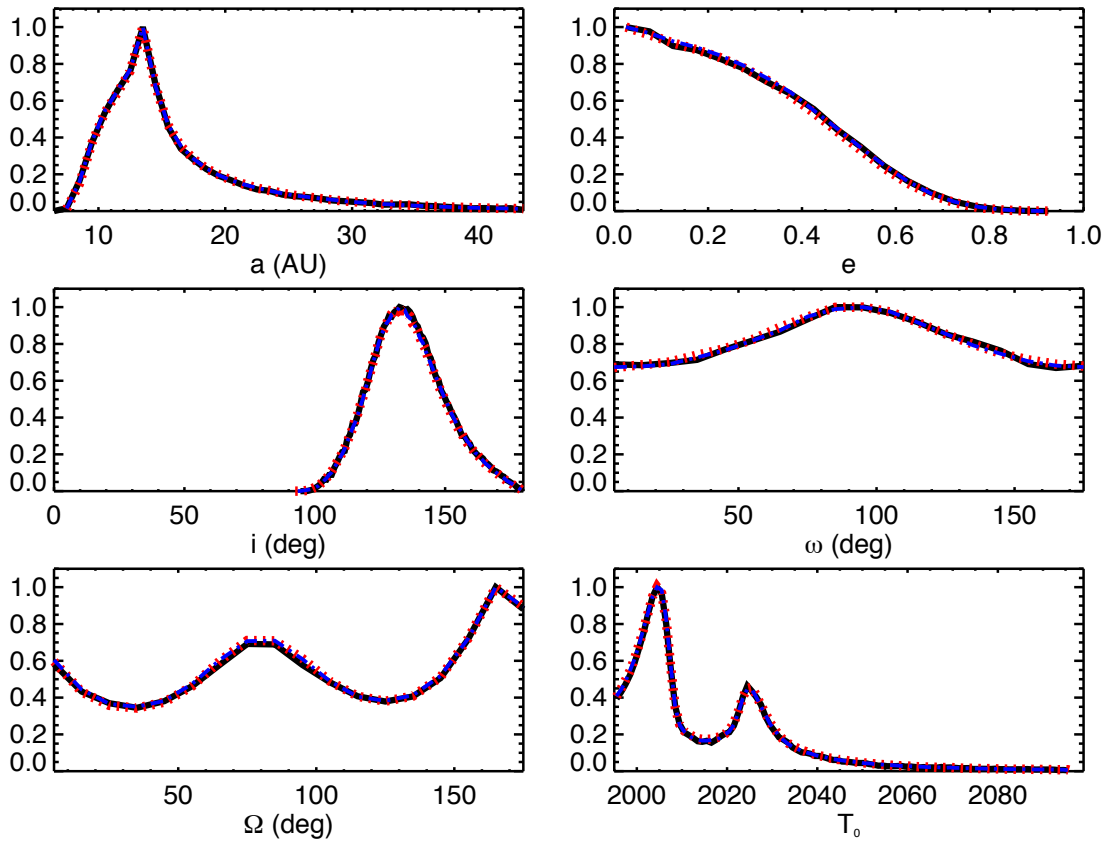
FIGURE 3.3: Normalized PDFs of the orbital parameters corresponding to orbits accepted by OFTI (red), Metropolis-Hastings MCMC (black), and Affine-Invariant MCMC (blue) for relative astrometry of 51 Eri b from its discovery in 2014 December to 2015 September. The PDFs produced by all methods are identical, differing only by shot noise.

3.3 Estimate of Performance

OFTI is a rejection-sampling method, meaning that it works by randomly sampling the parameter space of interest, then rejecting the sampled areas that do not match the data. As astrometry drawn from a larger fraction of the orbit becomes available, the orbit becomes more constrained, and the areas of parameter space that match the data shrink, so that OFTI becomes less efficient. A useful analogy for this phenomenon is throwing darts at a dartboard: when astrometry from only a small fraction of an orbit is available, many diverse orbits might fit the data, and a large fraction of the dartboard is acceptable, which results in a high acceptance rate. However, when more astrometry becomes available, a much smaller set of orbits will fit the data, and a much smaller fraction of the dartboard is acceptable, resulting in a lower acceptance rate.

Accordingly, OFTI is most efficient for astrometry covering a short fraction of an orbit, typically less than 15 % of the full orbital period. Because directly imaged exoplanets and brown dwarfs have large physical separations from their primary objects (greater
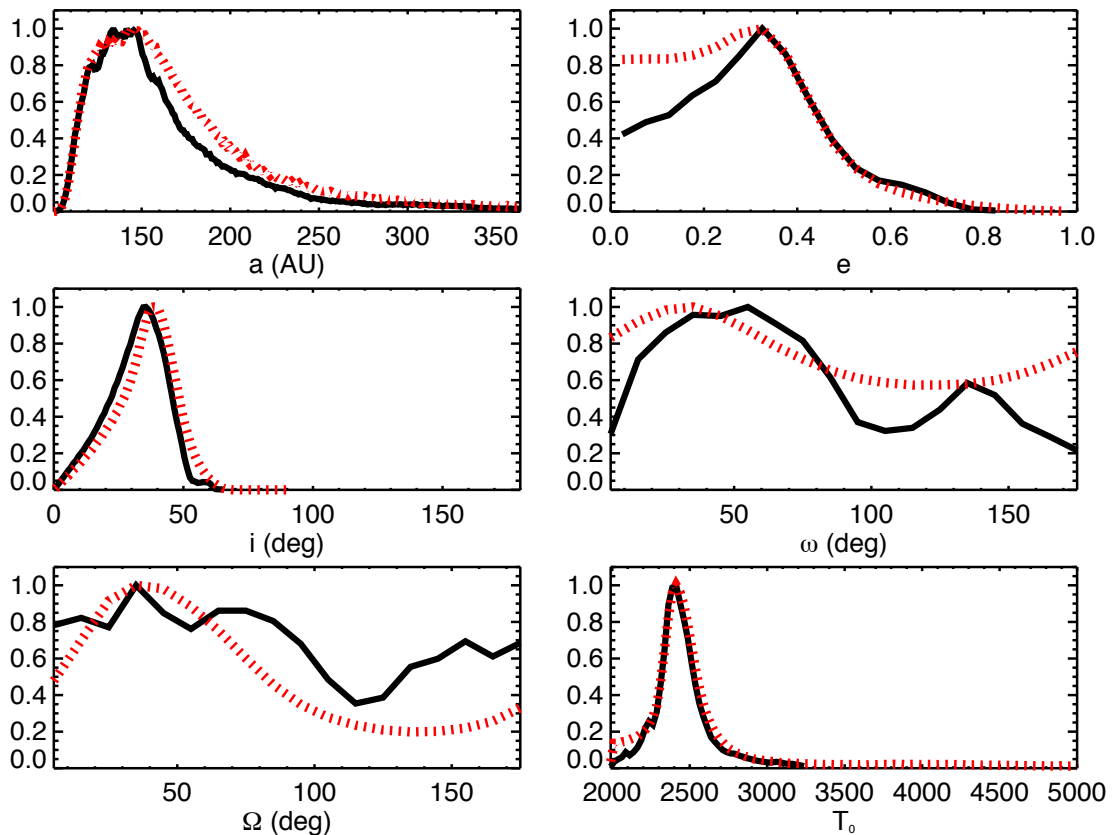
FIGURE 3.4: Normalized PDFs of the orbital parameters produced by OFTI (red) and MCMC (black) for astrometry of ROXs 42B b. After approximately 30 hours of running in parallel on 10 cores, the MCMC chains are still unconverged, while OFTI produced 10^6 permissible orbits in 134 minutes. The GR statistics for the MCMC chains plotted are all greater than 1.1, and the GR statistic for Ω is close to 1.5

than several au), OFTI is ideal for fitting the orbits of directly imaged systems, especially when the time spanned by direct imaging observations is short.

OFTI is also optimal when a quick estimate of the mean of a distribution is required. This will be particularly helpful in planning follow-up observations for space missions, as it allows to quickly estimate the optimal time for observations, also taking into account the possibility of the planet passing behind the star (see e.g. [56]). As Figure 3.5 shows, OFTI can converge on an estimate for the median of the 51 Eri b semi-major axis distribution within 5 % of the true median after fewer than 10^4 orbits are tested. While an implementation of MCMC would have to run to completion in order to avoid a biased estimate of the semi-major axis distribution, the independence of successive OFTI trials allows OFTI to converge on an unbiased estimate much faster.
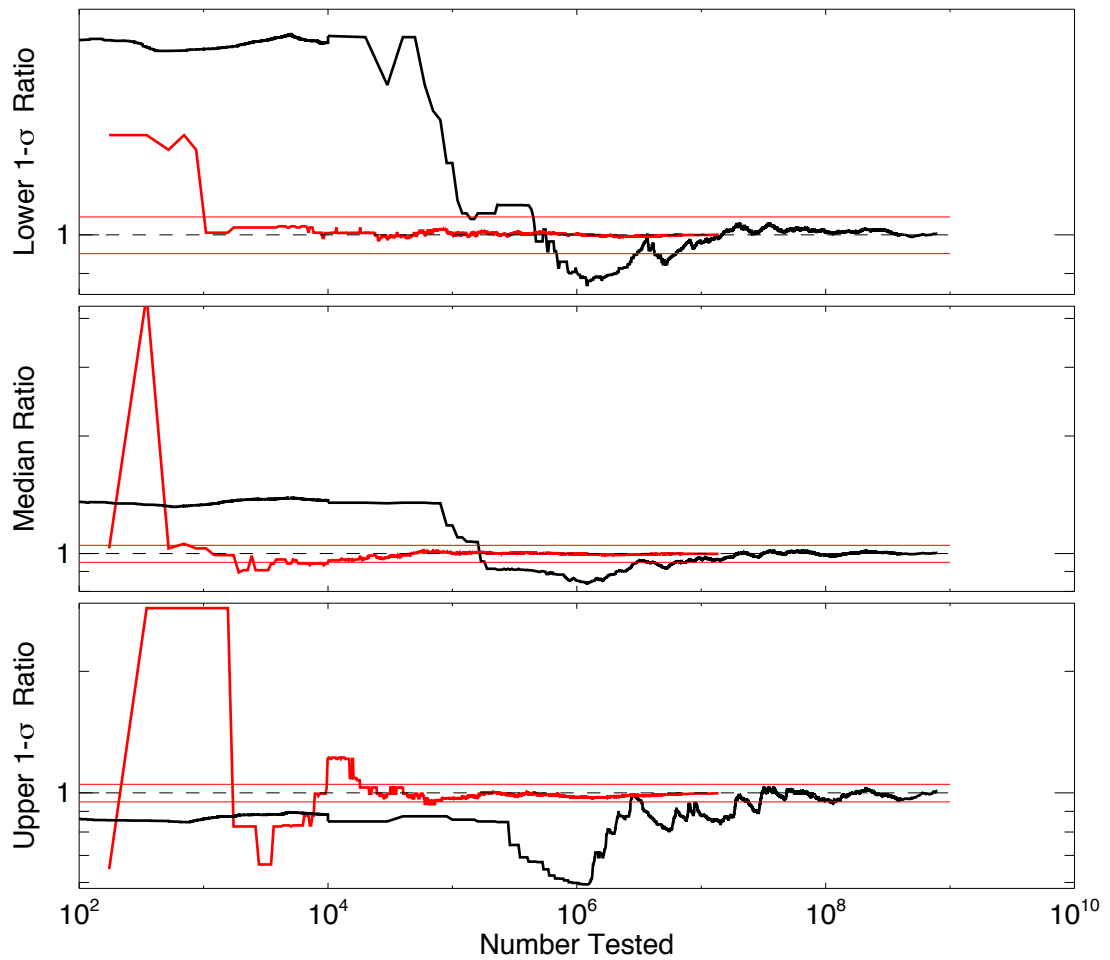
FIGURE 3.5: Ratios of the partial and final lower $1\,\sigma$ limit, median, and upper $1\,\sigma$ limit for one Metropolis-Hastings MCMC chain (black), and one OFTI run (red), computed for all published astrometry of 51 Eri b. OFTI converges on the appropriate median solution after testing approximately 10^4 sets of orbital elements, while MCMC continues to "wander" in a correlated fashion until accepting approximately 10^7 orbits. Red horizontal lines are located at ratios of 1.05 and 0.95, and a black dashed line is located at a ratio of 1.00.
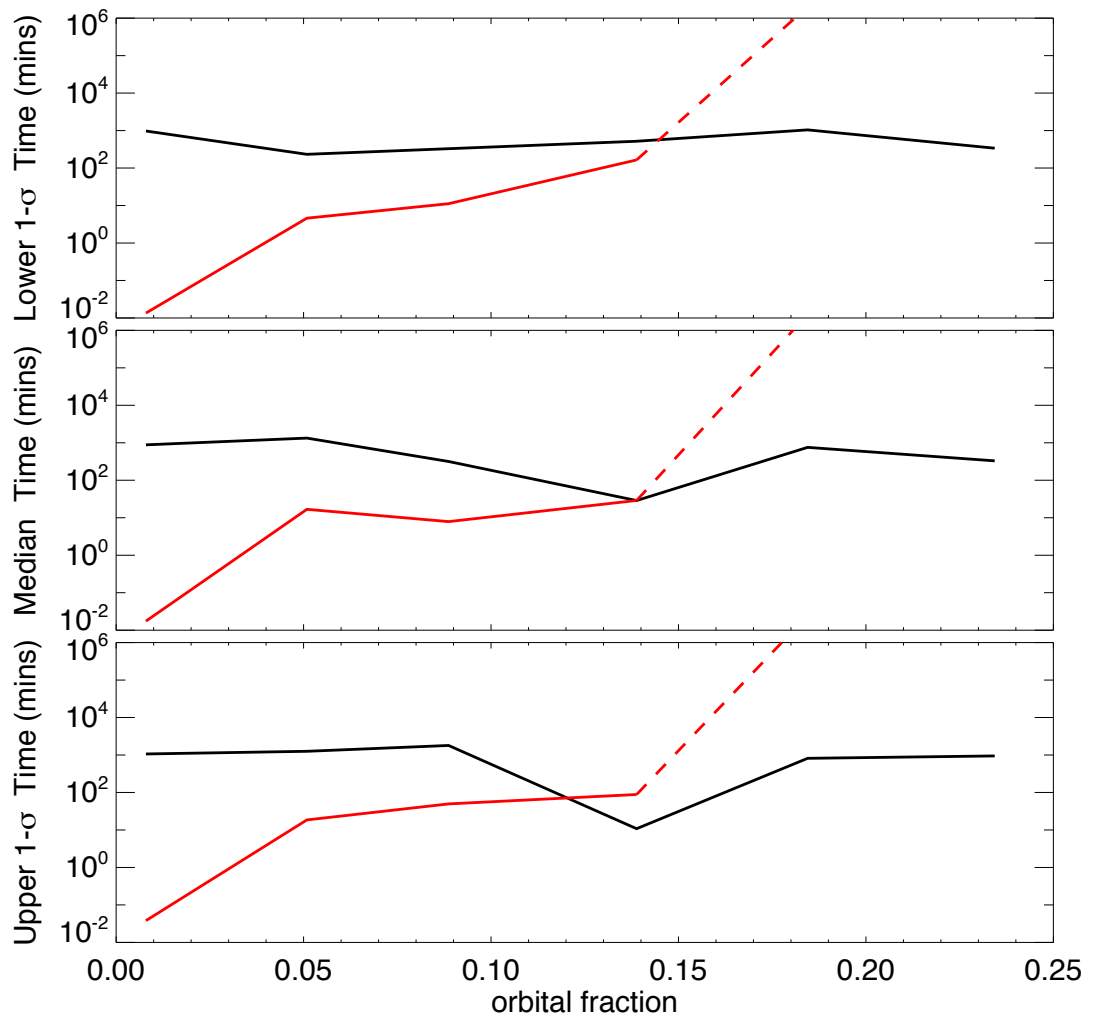
FIGURE 3.6: Runtime per CPU needed for OFTI (red) and MCMC (black) to determine (within 1% error) the lower 1σ limit, median, and upper 1σ limit of the complete a distribution, as a function of the orbital fraction covered by input astrometry of β Pic b. As orbital fraction decreases, OFTI performance improves, while MCMC performance slightly improves. For orbital fractions greater than 15 %, we extrapolated the depicted behavior from the time OFTI took to accept 50 orbits.
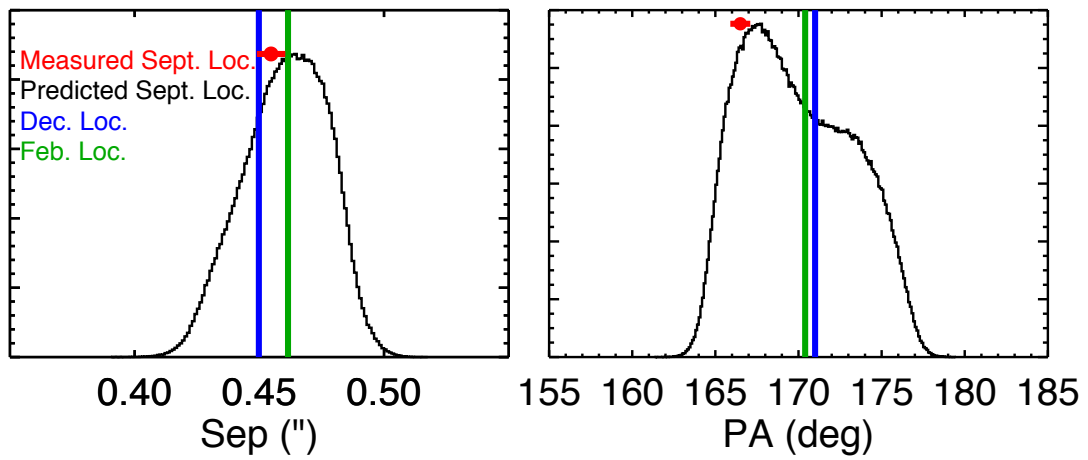
FIGURE 3.7: PDFs in separation and position angle (black curves) predicting the location of 51 Eri b on 2015 September 15, given all previously known epochs of astrometry. The vertical blue lines show the astrometric location of 51 Eri b on 2015 February 1, the green lines the location on 2014 December 18, and the red horizontal bars the measured ρ, θ.

Chapter 4

Applications

4.1 OFTI Fits Presented in Blunt et al 2017

In Blunt et al. 2017 **??**, we use OFTI to fit orbits to 10 sets of astrometry from directly imaged exoplanets, brown dwarfs, and low-mass stars in the literature. Each substellar object has at least two published epochs of astrometry. We chose mostly objects for which an orbital fit has not been calculated because the available astrometry covers a short fraction of the object's orbit. In performing these fits, we make the natural assumption that all objects are bound, and that all objects execute Keplerian orbits, as the chance of catching a common proper motion companion in the process of ejection or during the closest approach of two unassociated objects is particularly small.

We calculate fits using only the data available in the literature. Random and systematic errors in the astrometry available in the literature can bias these results. In particular, systematic errors in the measurement of plate scale or true north of the various instruments used to compile a single astrometric data set can significantly change orbit fits. Sharp apparent motion due to astrometric errors is likely to be fit as a higher eccentricity orbit; more astrometric data are needed to identify outliers of this nature.

For each substellar object, we compiled relative astrometry, distances, and individual object mass estimates from the literature, then ran OFTI on these data (see Appendix in [3]).

To illustrate our results, for each orbit, we provide:

- A table listing the maximum probability (maximum product of χ^2 probability and prior probabilities), minimum χ^2, median, 68 % confidence interval, and 95 % confidence interval orbital elements

- A triangle plot showing posterior distributions for each orbital element and 2-dimensional covariances for each pair of orbital elements

- A 3-panel plot showing 100 orbits drawn from the posterior distributions

4.1.1   GJ 504

GJ 504 b is the coldest and bluest directly-imaged exoplanet to date, and one of the lowest mass. Its discovery was reported by Kuzuhara et al. [34], who also perform a rejection-sampling orbit fit similar to OFTI [30]. Results are shown in Table 4.1 and Figures 4.1 and 4.2. Our results are consistent with the posterior distributions they find (noting that Kuzuhara et al. [34] have used a flat prior in eccentricity). Using a linearly descending prior in eccentricity, we find a median semi-major axis of 48 au, with 68 % confidence between 39 and 69 au, and a corresponding period of 299 years, with 68 % confidence between 218 and 523 years. We also note that Kuzuhara et al. [34] find an e posterior that decreases with eccentricity, as we do for OFTI calculations performed assuming both a uniform eccentricity prior and a linearly descending eccentricity prior.

We calculated fraction of orbital coverage by dividing the time spanned by observations by the 68 % confidence limits of the posterior distribution in period produced by OFTI. The calculated orbital fraction for the orbit of GJ 504 b is $0.4\,^{+0.1}_{-0.2}\,\%$.

To illustrate the impact of our choice of eccentricity prior on the results, we performed another fit to the astrometry of GJ 504 b using a uniform, rather than a linearly descending, prior in eccentricity. The results are shown in Figure 4.3. The use of a different eccentricity prior changes the eccentricity posterior PDF, but does not significantly affect the other posterior PDFs. For example, when a linearly descending eccentricity prior is used, the semi-major axis posterior is $48\,^{+22}_{-9}$ au, and when a uniform eccentricity prior is used, the posterior shifts to $47\,^{+26}_{-11}$ au.

4.1.2   HD 1160

HD 1160 A hosts two known companions: HD 1160 B, a low-mass object at the stellar/brown dwarf boundary [23], and HD 1160 C, an M3.5 star at a wider projected separation than HD 1160 B [47]. We compute fits to both the orbits of HD 1160 B and HD 1160 C with respect to HD 1160 A. Preliminary orbital fits were provided by Nielsen et al. [48], but an updated fit including the latest astrometry published in Maire et al. [39] has not been computed. The results of our fits are shown in Tables 4.2 and 4.3 and Figures 4.4 - 4.7. Because HD 1160 B and C are non-planetary companions, we used a uniform prior in e, rather than the empirically derived linearly descending prior

	unit	max probability	min χ^2	median	68% conf. range	95% conf. range
a	au	44.48	67.24	48	39-69	31-129
P	yr	268.56	508.23	299	218-523	155-1332
e		0.0151	0.1519	0.19	0.05-0.40	0.01-0.62
i	°	142.2	131.7	140	125-157	111-171
ω	°	91.7	4.9	95	31-151	4-176
Ω	°	133.7	61.6	97	46-146	8-173
T_0	yr	2228.11	2419.96	2145.10	2068.06-2310.13	2005.07-2825.03

TABLE 4.1: Orbit of GJ 504 b with respect to GJ 504 A. Note: Ω and ω have been wrapped between 0 and 180°, and T_0 has been wrapped between 1995 and 1995 + 1 period. The maximum probability orbit was calculated by multiplying the output χ^2 likelihood by the priors, and taking the orbit with the maximum product. The acceptance rate was 0.13 %.
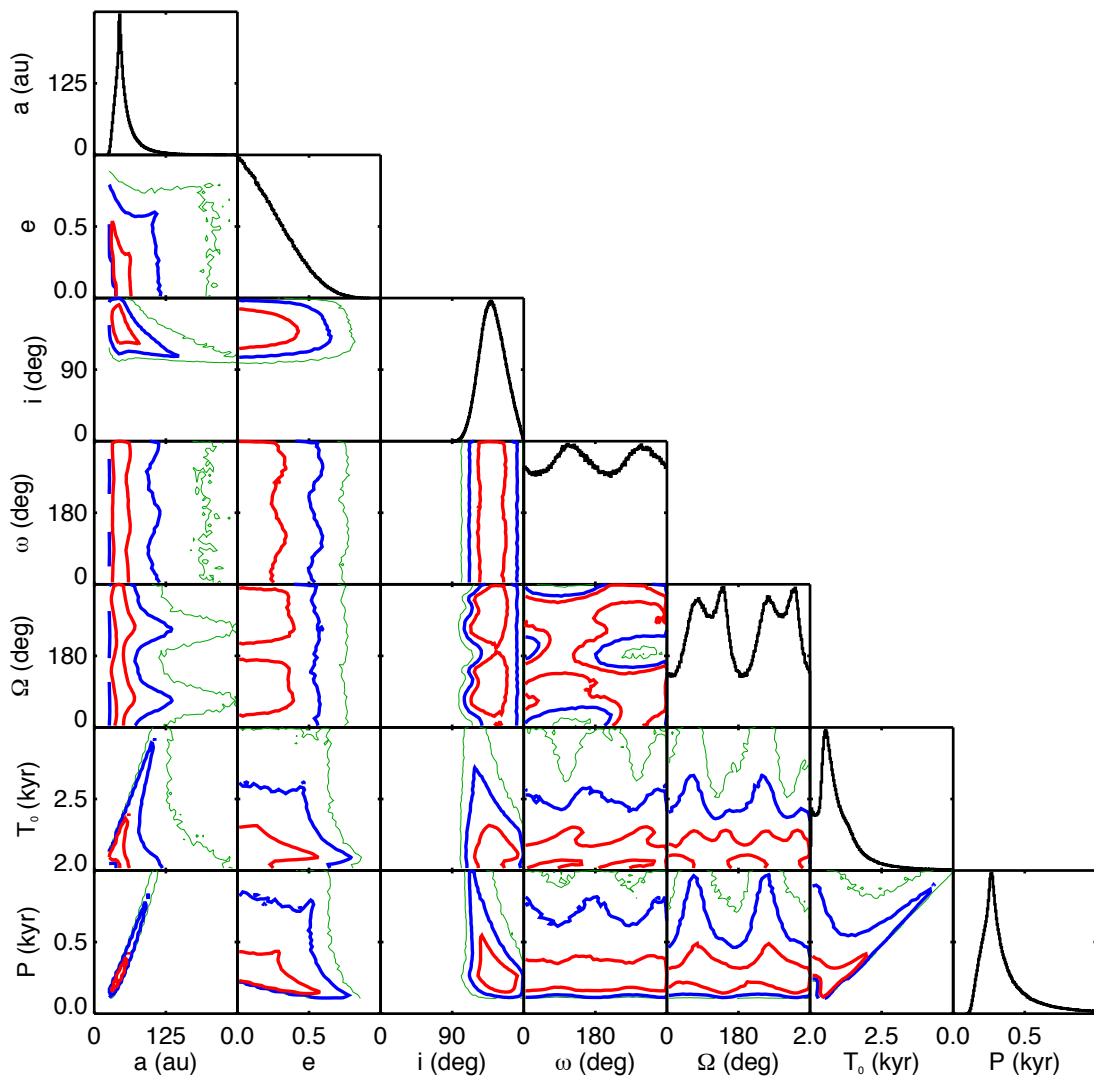

FIGURE 4.1: Posterior PDFs for the orbit of GJ 504 b with respect to GJ 504 A. Black lined panels on the diagonal show the posterior probability distributions for each of the orbital parameters, while off-diagonal plots show two-dimensional covariance contour plots. Red lines depict 68 % contours, blue lines depict 95 % contours, and green lines depict 99 % contours.
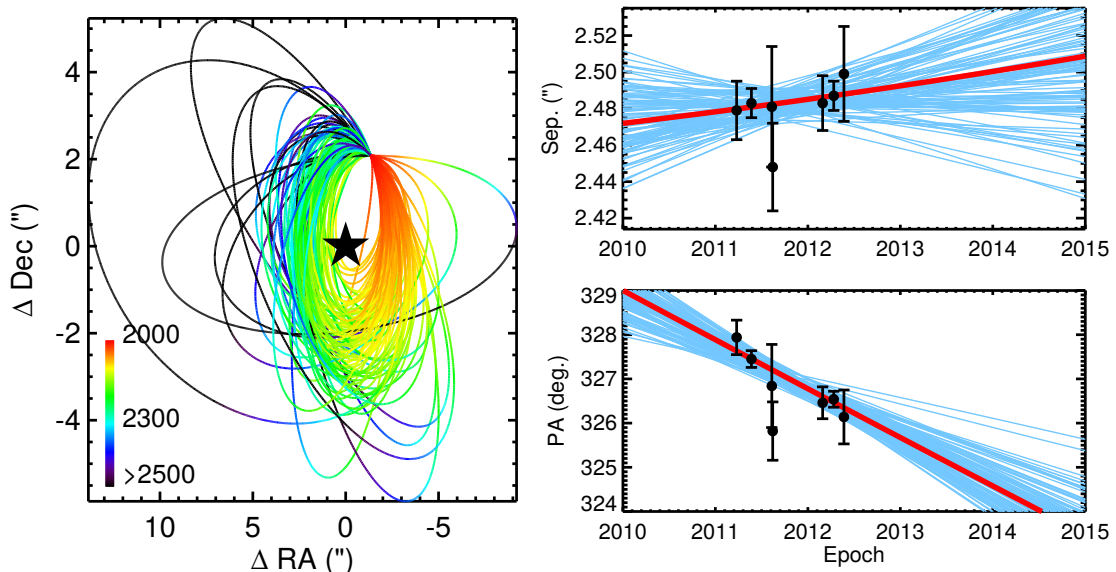
FIGURE 4.2: 100 orbits fit to relative astrometry of GJ 504 b with respect to GJ 504 A, randomly selected from OFTI posterior PDFs. Left: orbital motion of GJ 504 b with respect to GJ 504 A over an orbital period. As elapsed time since the most recent observational epoch increases, the color of the orbital track changes from red to green to black (see colorbar in lower left corner). The black star indicates the primary. Right: relative separations (top) and position angles (bottom), together with the observed measurements and errors (black points with error bars), and minimum χ^2 orbit (red line). These orbits are the same as the orbits plotted in the left panel.

used for exoplanets. This choice is supported by evidence that the empirical eccentricity distribution of long-period stellar binaries is approximately uniform (e.g. [15]).

For HD 1160 B, the fraction of orbital coverage is $2.5^{+2.2}_{-1.8}\%$, while for HD 1160 C, the fraction of orbital coverage is $0.11 \pm 0.06\%$.

OFTI constrains the range of possible inclination angles for the orbit of HD 1160 B tightly, with a 68% confidence interval of $96\text{-}119\,^{\circ}$, indicating close to an edge-on orbit. We find a semi-major axis of 77^{+96}_{-27} au, and a period of 479^{+1148}_{-227} years. A high eccentricity is favored. As seen in Figure 4.5, the minimum χ^2 orbit passes through all $1\,\sigma$ error bars in ρ and θ, allowing OFTI to converge on a set of permissible orbits in fewer iterations than, for example, the orbit of η Tel B, whose data set contains several clear outliers (see Section 4.6).

The fit favors a more face-on orbit for HD 1160 C than for HD 1160 B, returning an inclination angle of $146^{+17}_{-18}\,^{\circ}$. The probability that the inclination angle of HD 1160 B is within $10\,^{\circ}$ of the inclination angle of HD 1160 C is 8%. It is fairly typical for triple stellar systems to be non-coplanar (e.g. [19], [62]), so this result is plausible. In keeping with the larger projected separation of HD 1160 C, we find a larger semi-major axis, 651^{+432}_{-160} au, and period, $11,260^{+12,930}_{-3,898}$ years, for HD 1160 C compared to HD 1160 B.
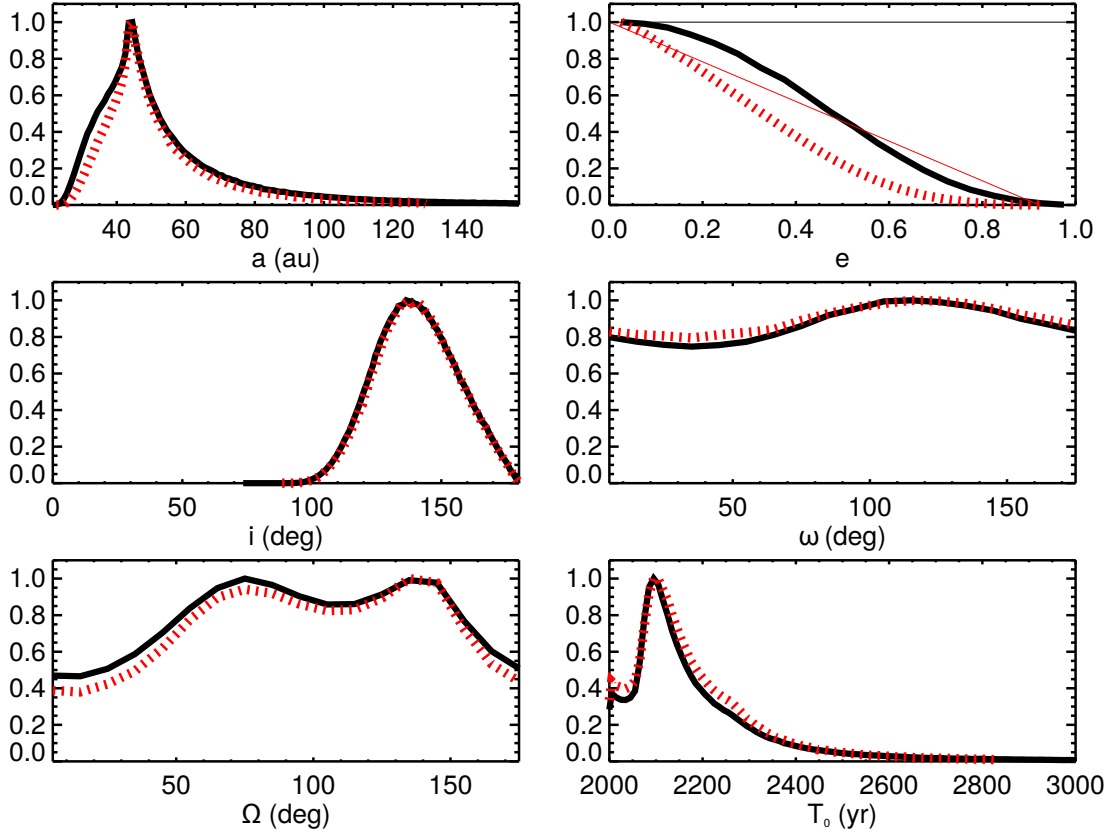
FIGURE 4.3: Posterior PDFs for the orbit of GJ 504 b, calculated using a linearly descending prior in eccentricity (red), and a uniform prior in eccentricity (black). The choice of prior strongly affects the eccentricity posterior, but the other orbital element posteriors are generally the same. The largest change seen is in semi-major axis, where the distribution shifts from 48^{+22}_{-9} au to 47^{+26}_{-11} au when changing the linearly descending eccentricity prior to a uniform one. The two relevant eccentricity priors are plotted in the eccentricity panel as thin red and black lines.

	unit	max probability	min χ^2	median	68% conf. range	95% conf. range
a	au	45.27	77.86	77	50-173	42-834
P	yr	218.02	482.21	479	252-1627	194-17134
e		0.8119	0.2550	0.77	0.35-0.94	0.05-0.98
i	°	109.3	98.2	103	96-119	92-149
ω	°	10.2	99.9	96	39-143	6-174
Ω	°	66.1	61.1	63	38-91	9-169
T_0	yr	2137.84	2138.27	2220.06	2131.28-2796.96	2087.36-9871.18

TABLE 4.2: Orbit of HD 1160 B with respect to HD 1160 A. The acceptance rate was 0.24 %.
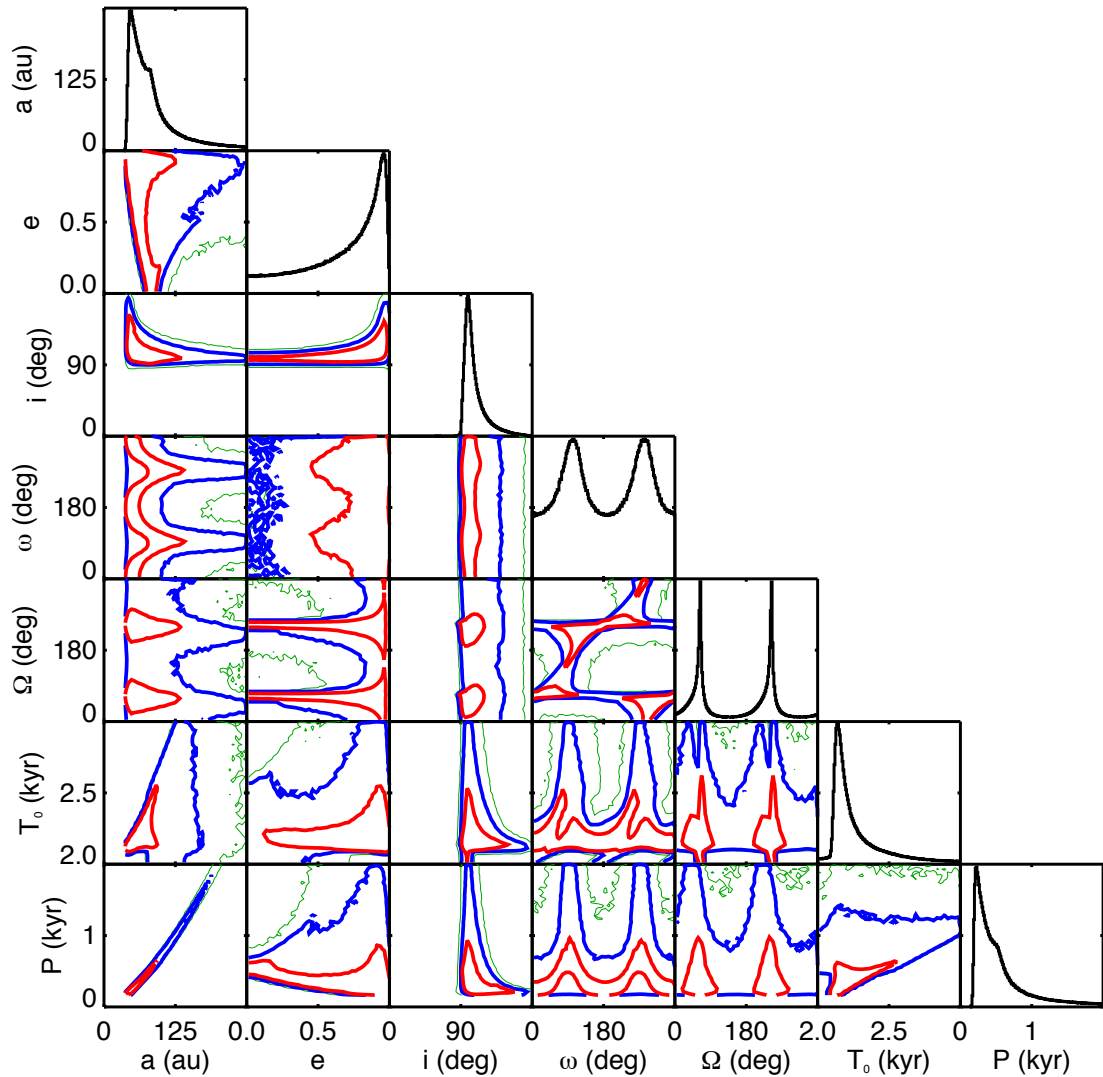
FIGURE 4.4: Triangle plots for the orbit of HD 1160 B with respect to HD 1160 A. See Figure 4.1.

	unit	max probability	min χ^2	median	68% conf. range	95% conf. range
a	au	1631.43	2512.52	651	491-1083	372-2454
P	yr	45119.44	80174.59	11260	7362-24190	4852-82443
e		0.6286	0.8110	0.33	0.11-0.60	0.02-0.82
i	°	136.1	170.9	146	128-163	110-174
ω	°	31.4	93.1	84	28-150	4-176
Ω	°	25.2	56.4	62	20-148	3-177
T_0	yr	46827.45	2374.57	3812.12	2915.07-8680.52	2195.37-31708.72

TABLE 4.3: Orbit of HD 1160 C with respect to HD 1160 A. Note: The acceptance rate was 0.006 %.
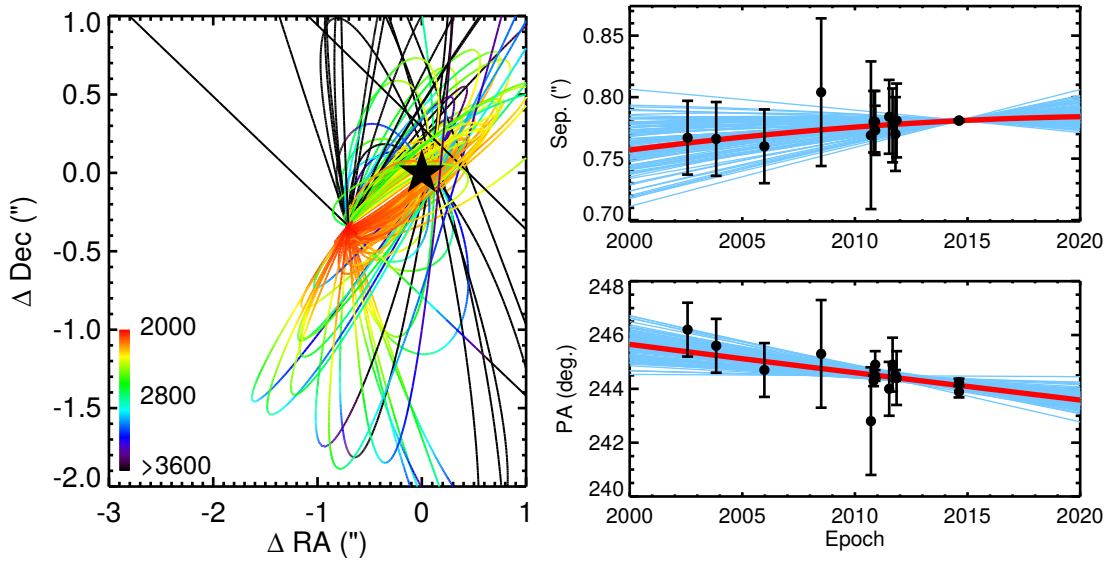
FIGURE 4.5: Depictions of 100 likely orbits fit to relative astrometry of HD 1160 B with respect to HD 1160 A. See Figure 4.2.

	unit	max probability	min χ^2	median	68% conf. range	95% conf. range
a	au	2.01	9.96	3	2-8	2-35
P	yr	8.71	82.70	23	11-86	7-735
e		0.9133	0.8965	0.75	0.31-0.95	0.05-0.99
i	°	75.2	85.0	83	66-93	34-117
ω	°	151.1	104.0	95	39-145	6-174
Ω	°	168.4	8.3	157	51-166	4-177
T_0	yr	1998.44	2061.23	2005.47	1998.34-2034.01	1995.48-2338.70

TABLE 4.4: Orbit of HIP 79797 Bb with respect to HIP 79797 Ba. Note: The acceptance rate was 13.8%.

4.1.3   HIP 79797

HIP 79797 Ba and HIP 79797 Bb are a close binary brown dwarf system orbiting the A star HIP 79797 A, first detected as an unresolved companion by Huélamo et al. [29], and resolved into a binary by Nielsen et al. [48]. Nielsen et al. [48] perform a preliminary orbit fit using MCMC, but note that the MCMC fit was un-converged. Results are shown in Table 4.4 and Figures 4.8 and 4.9. Like Nielsen et al. [48], our OFTI fit favors an edge-on orbit ($i = 83^{+10}_{-17}$°), but we find a significantly smaller semi-major axis (3^{+5}_{-1} au, where Nielsen et al give a semi-major axis of 25^{+97}_{-19} au) and corresponding period (23^{+63}_{-12} years, where Nielsen et al. [48] give a period of 380^{+3700}_{-330} years). Our fit favors high eccentricity orbits. Again, we use a uniform prior in eccentricity. The calculated orbital fraction for the orbit of HIP 79797 Ba and HIP 79797 Bb is 10^{+11}_{-8}%.
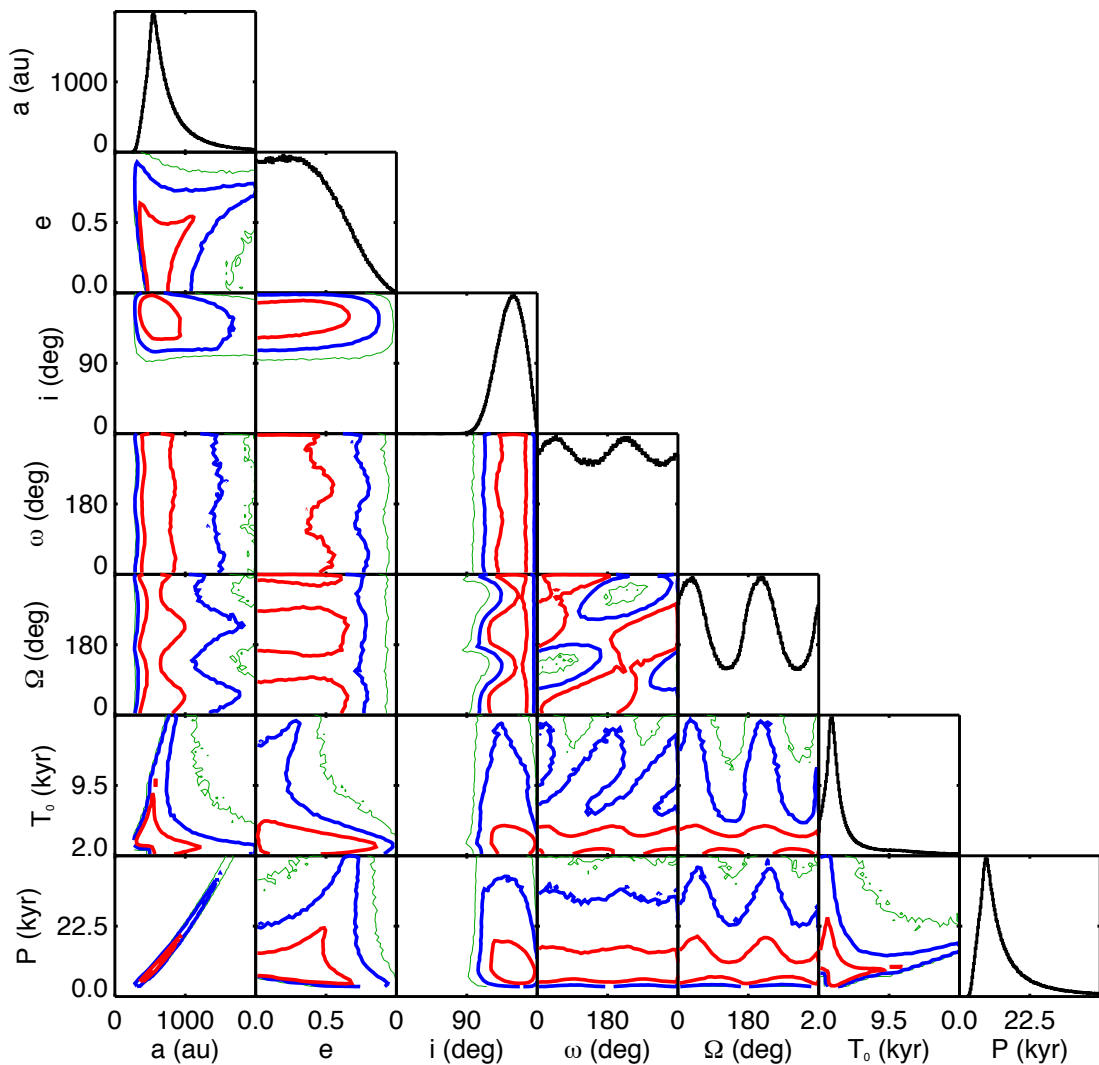
FIGURE 4.6: Triangle plots for the orbit of HD 1160 C with respect to HD 1160 A. See Figure 4.1.

4.1.4   HR 3549

HR 3549 B is a brown dwarf orbiting the A0V star HR 3549 A, discovered by Mawet et al. [40], and followed up by Mesa et al. [41]. Mesa et al. [41] use a LSMC technique to constrain the orbit of HR 3549, and provide orbital elements for three orbits with greatest likelihood (least χ^2). While minimization algorithms like these are effective at finding local maxima in likelihood space, OFTI produces full Bayesian posteriors that show probability, rather than likelihood. Our OFTI fit, in contrast to that of Mesa et al. [41], makes use of both astrometry points Mesa et al. [41] provide, rather than just one, and uses a Gaussian prior in mass with full width at half maximum (FWHM) equal to 5 % of the reported value in Mesa et al. [41], rather than a fixed value. Our results are provided in Table 4.5 and Figures 4.10 and 4.11. We find a semi-major axis of $94\,^{+65}_{-28}$ au,
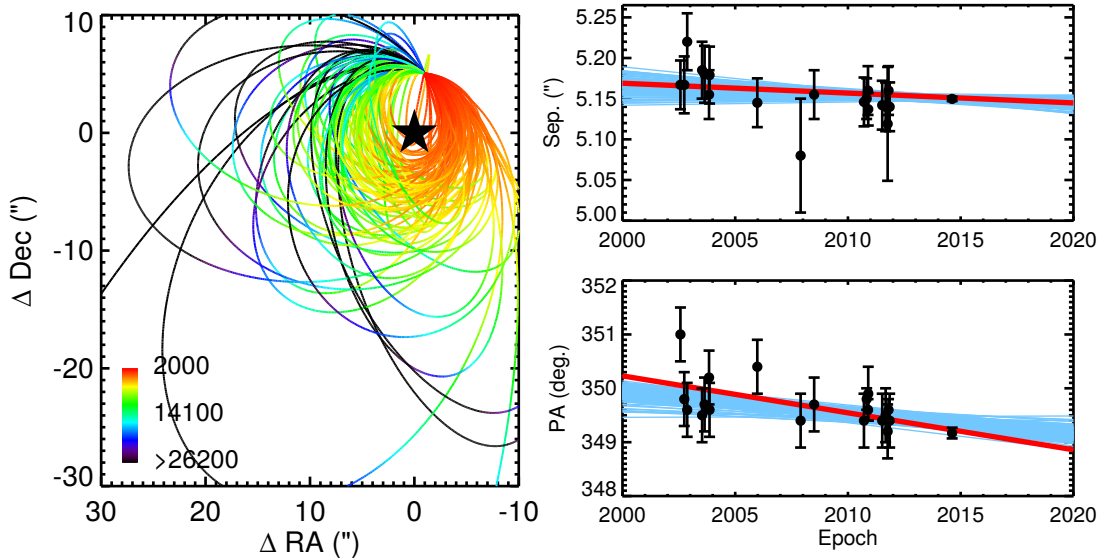
FIGURE 4.7: Depictions of 100 likely orbits fit to relative astrometry of HD 1160 C with respect to HD 1160 A. See Figure 4.2.

	unit	max probability	min χ^2	median	68% conf. range	95% conf. range
a	au	85.84	83.73	94	66-159	50-360
P	yr	520.01	496.86	592	346-1303	231-4461
e		0.5103	0.4797	0.47	0.16-0.75	0.02-0.92
i	°	138.5	138.1	130	111-152	96-170
ω	°	136.8	167.3	87	26-152	4-176
Ω	°	172.6	14.0	77	13-168	2-178
T_0	yr	2094.84	2105.86	2115.38	2078.47-2319.26	2030.61-3633.32

TABLE 4.5: Orbit of HR 3549 B with respect to HR 3549 A. Note: The acceptance rate was 2.59 %.

which contains one of the semi-major axis values reported by Mesa et al. [41] (133.2 au), while the other two semi-major axis values Mesa et al. [41] report (299.7 and 441.2 au) are at 1.7 and 2.9 σ, respectively, of our semi-major axis distribution. Like Mesa et al. [41], we find that most values of eccentricity, and values of $i > 90\,°$, are consistent with the astrometry, a reflection of the fact that the astrometry covers only a fraction of the full orbital arc ($0.5\,^{+0.4}_{-0.3}\,\%$).

4.1.5 2M 1207

2MASSW J1207334-393254 b (hereafter 2M 1207 b) is a planetary mass companion orbiting 2M 1207 A, a brown dwarf with mass approximately three times that of 2M 1207 b. 2M 1207 b was first discovered using the Very Large Telescope with NACO by Chauvin et al. [8]. It was followed up first by Song et al. [59], who confirmed the common proper
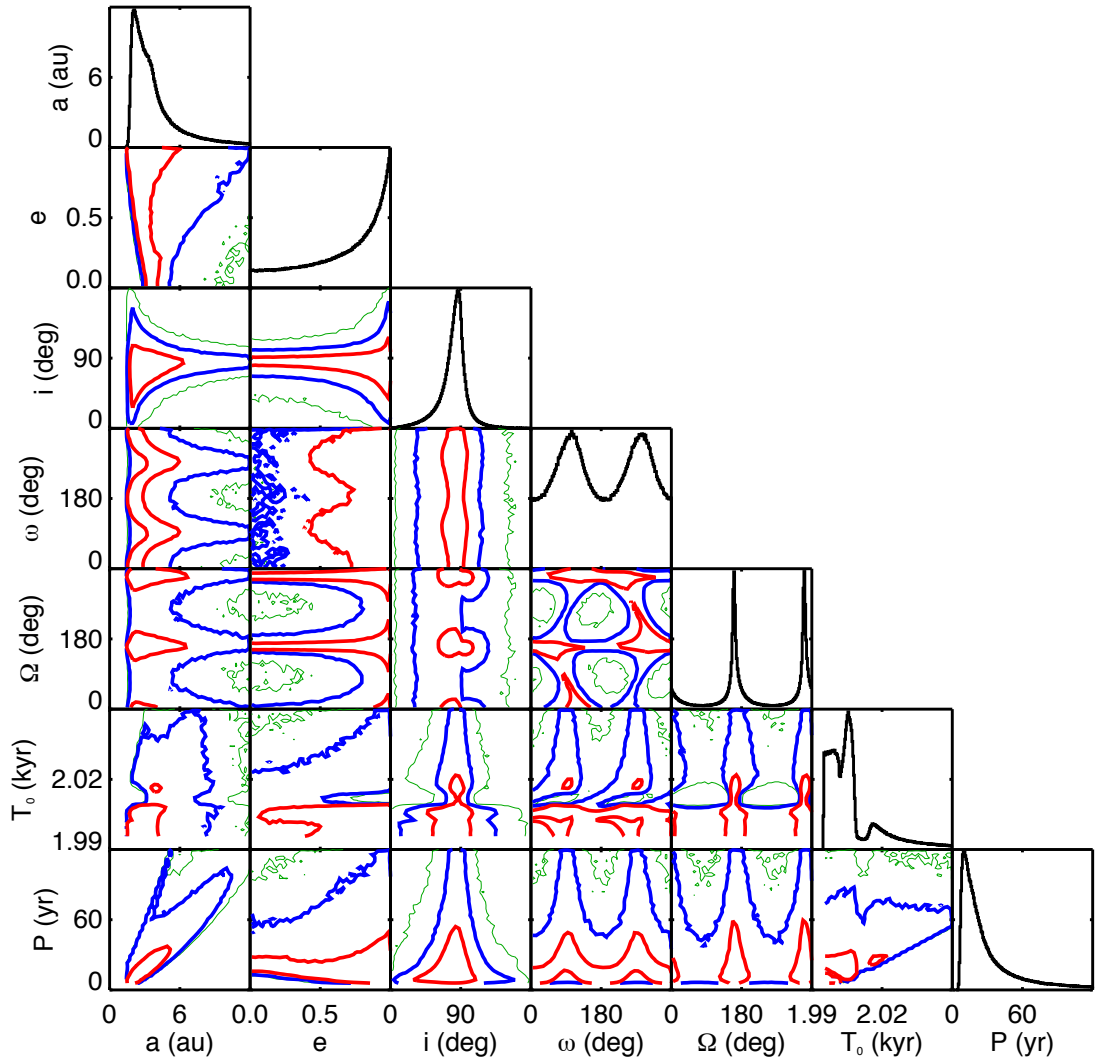
FIGURE 4.8: Triangle plots for the orbit of HIP 79797 Bb with respect to HIP 79797 Ba.
See Figure 4.1.

motion of the pair, establishing 2M 1207 b as a bound companion, and again by Mo-
hanty et al. [43]. Orbital fits are shown in Table 4.6 and Figures 4.12 and 4.13. Using a
linearly descending prior in eccentricity, we find a median semi-major axis of 46 au, with
68 % confidence between 31 and 84 au. We only loosely constrain the range of possible
inclination angles, and determine that high eccentricity (> 0.8) orbits are dispreferred.
The median orbital period is 1,782 years, with 95 % confidence between 633 years and
20,046 years. The calculated orbital fraction for the orbit of 2M 1207 b is $0.06^{+0.05}_{-0.03}$ %.

4.1.6 κ And

κ And B is a substellar companion orbiting the late B star κ And. The discovery of
κ And B was first reported by Carson et al. [7], and followed up by Bonnefoy et al. [4].
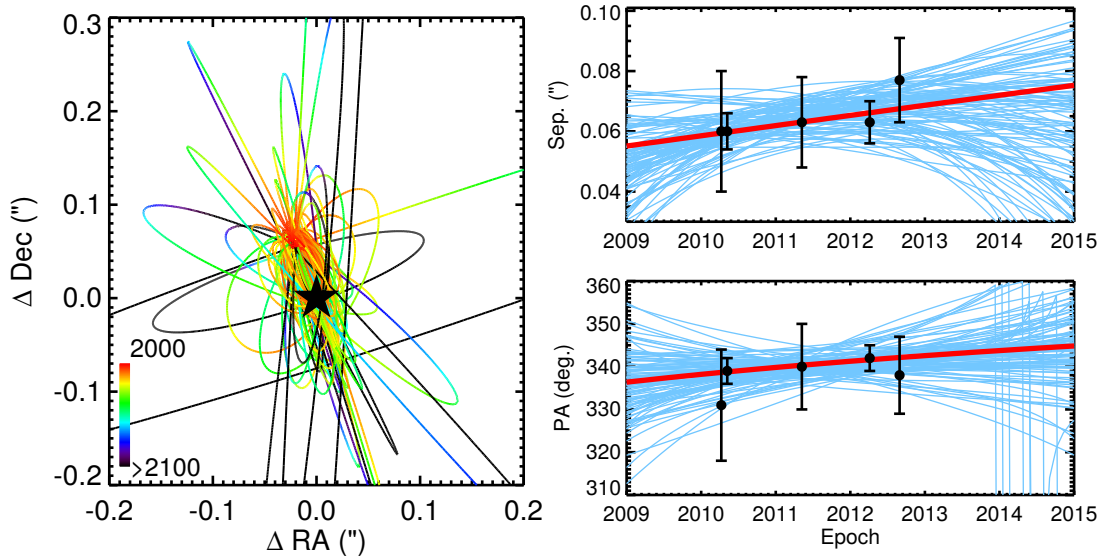
FIGURE 4.9: Depictions of 100 likely orbits fit to relative astrometry of HIP 79797 Bb with respect to HIP 79797 Ba. See Figure 4.2. Note: the vertical bars in the bottom right plot result from PA crossing 360 °.

	unit	max probability	min χ^2	median	68% conf. range	95% conf. range
a	au	35.26	91.88	46	31-84	24-231
P	yr	1153.44	4648.27	1782	974-4413	633-20046
e		0.2226	0.5226	0.49	0.15-0.83	0.02-0.98
i	°	41.6	41.5	69	36-109	13-150
ω	°	141.4	161.6	90	29-151	4-176
Ω	°	129.6	1.9	119	52-146	7-174
T_0	yr	2424.39	2172.58	2683.34	2285.03-4277.65	2107.69-12883.36

TABLE 4.6: Orbit of 2M 1207 b with respect to 2M 1207 A. Note: The acceptance rate was 13.99 %.

Results are shown in Table 4.7 and Figures 4.14 and 4.15. Using a linearly descending prior in eccentricity, we find a median semi-major axis of 77 au, with 68 % confidence between 54 and 123 au. Eccentricity remains mostly unconstrained after our analysis, but inclination is determined to be between 59 ° and 159 ° with 95 % confidence. The median orbital period is 378 years, with 95 % confidence between 144 years and 2,033 years. The calculated orbital fraction for the orbit of κ And B is $0.2^{+0.2}_{-0.1}$ %.

4.1.7 η Tel

η Tel B is a brown dwarf orbiting the A0V star η Tel A ([36], [44]). Results are shown in Table 4.8 and Figures 4.16 and 4.17. We find a median semi-major axis of 192 au, with 68 % confidence between 125 and 432 au. The corresponding median period is 1,493 years, with 68 % confidence between 781 and 5,028 years. OFTI produced a well-constrained posterior in inclination angle, with 95 % of orbits having an inclination angle
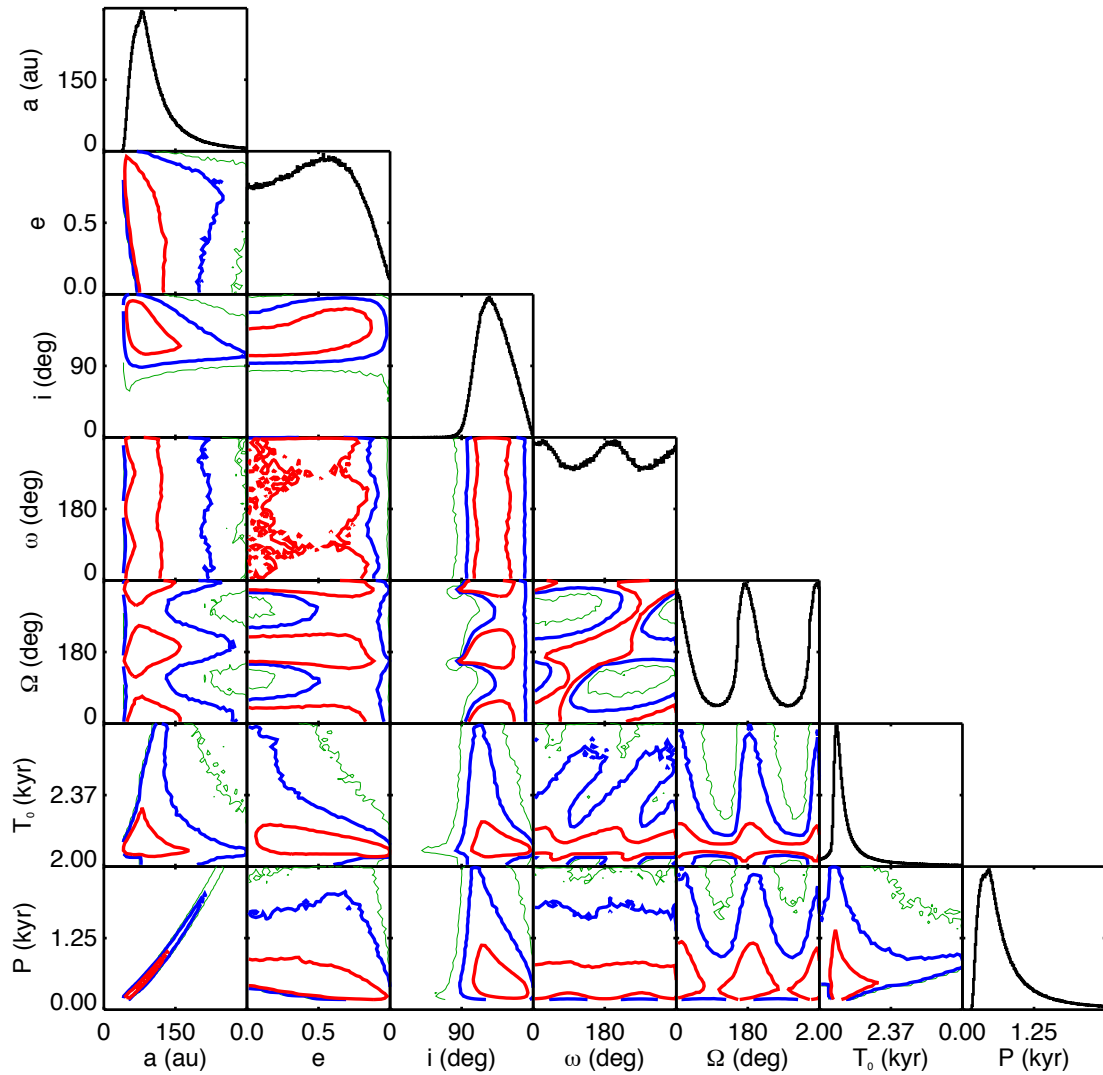
FIGURE 4.10: Triangle plots for the orbit of HR 3549 B with respect to HR 3549 A.
See Figure 4.1.

	unit	max probability	min χ^2	median	68% conf. range	95% conf. range
a	au	184.96	184.96	77	54-123	40-236
P	yr	1385.97	1385.97	378	223-768	144-2033
e		0.8908	0.8908	0.41	0.12-0.70	0.02-0.85
i	°	116.6	116.6	101	83-125	59-159
ω	°	138.7	138.7	112	29-159	3-177
Ω	°	67.8	67.8	63	49-84	26-127
T_0	yr	2040.10	2040.10	2065.27	2043.38-2188.31	2015.35-2858.45

TABLE 4.7: Orbit of κ And B with respect to κ And B. Note: The acceptance rate
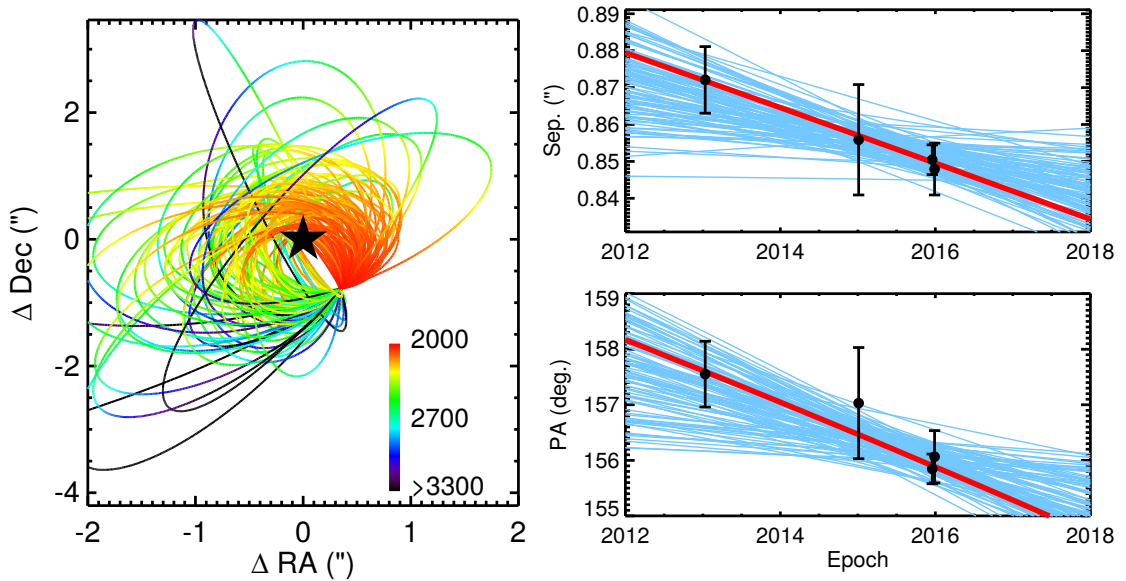was 0.02 %.

FIGURE 4.11: Depictions of 100 likely orbits fit to relative astrometry of HR 3549 B with respect to HR 3549 A. See Figure 4.2.

	unit	max probability	min χ^2	median	68% conf. range	95% conf. range
a	au	206.39	207.86	192	125-432	106-2091
P	yr	1600.73	1640.25	1493	781-5028	612-53621
e		0.9084	0.0354	0.77	0.34-0.96	0.05-1.00
i	°	88.4	87.4	86	72-96	40-120
ω	°	121.8	165.6	98	37-146	5-175
Ω	°	169.8	167.4	165	42-170	3-178
T_0	yr	2851.39	3623.16	2669.33	2391.73-4459.40	2263.35-26828.14

TABLE 4.8: Orbit of η Tel B with respect to η Tel A. Note: The acceptance rate was 0.00002 %.

between $40\,°$ and $120\,°$. Several data points are outliers, which results in a comparatively low orbital acceptance rate of $0.002\,\%$. We use a uniform prior in eccentricity. The calculated orbital fraction for the orbit of η Tel B is $0.7\,^{+0.7}_{-0.5}\,\%$.

4.1.8 2M 0103-55

2MASS J01033563-5515561 (AB) b (hereafter 2M 0103-55 (AB) b) is a 12-14 Jupiter-mass object in orbit with respect to 2M 0103-55 (AB), a binary consisting of two low mass stars [13]. Delorme et al. [13] first reported the discovery of 2M 0103-55 (AB) b, and provide two epochs of astrometry. Results are shown in Table 4.9 and Figures 4.18 and 4.19. Two epochs of astrometry is generally too short of a baseline for the two implementations of MCMC discussed in this work to converge within the timescale of a few days, but OFTI quickly returns the appropriate posteriors. Using a linearly descending prior in eccentricity, we find a semi-major axis of 102 au, with 68 % confidence
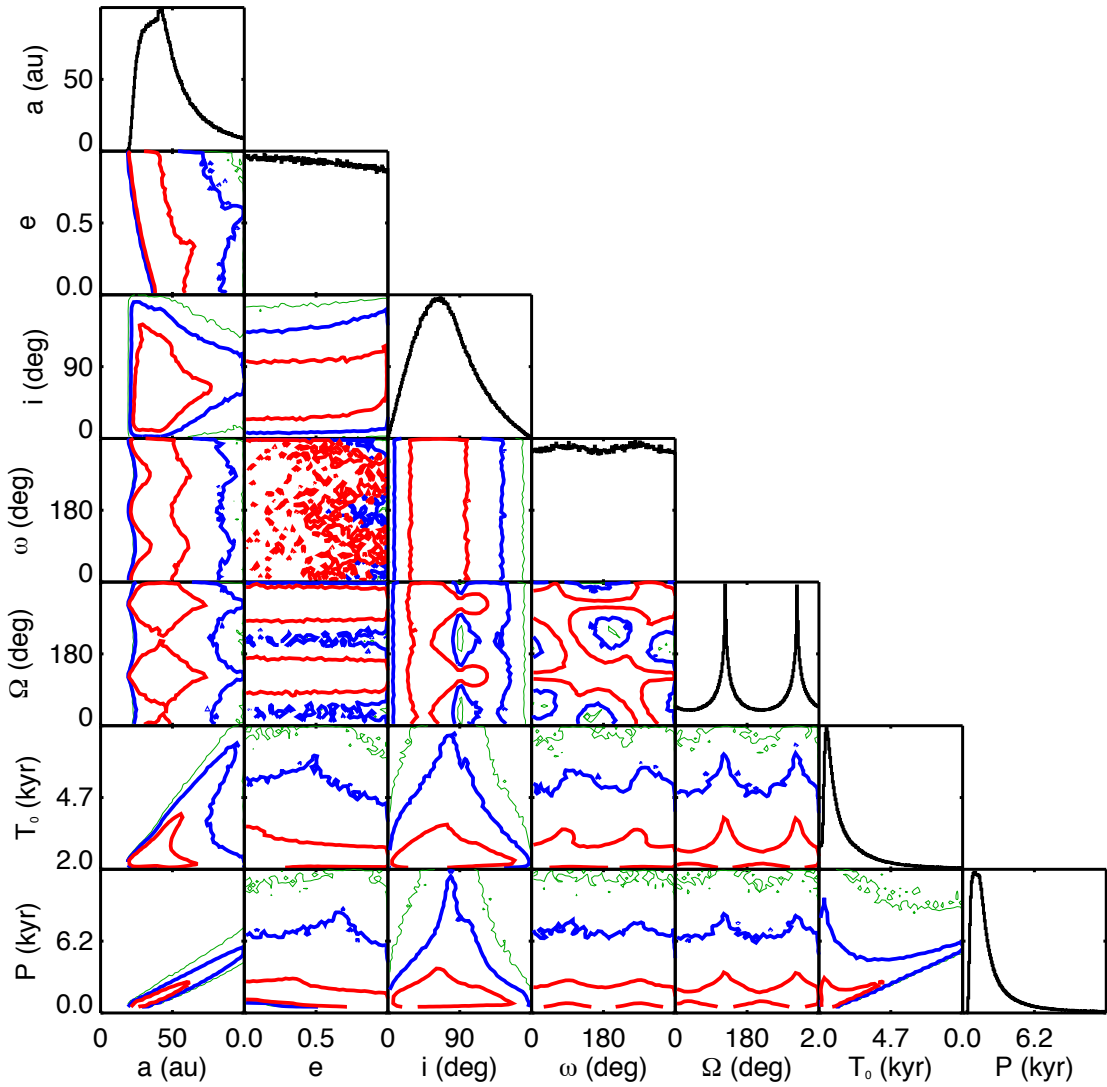
FIGURE 4.12: Triangle plots for the orbit of 2M 1207 b with respect to 2M 1207 A.
See Figure 4.1.

between 75 and 149 au, and a corresponding period of 1,682 years, with 68 % confidence between 1,054 and 2,990 years. OFTI also returns a firm lower limit on inclination angle, with 95 % of orbits having inclination angles greater than 112 °. The calculated orbital fraction for the orbit of 2M 0103 (AB) b is $0.6^{+0.4}_{-0.3}$ %.

4.1.9   CD-35 2722

CD-35 2722 B is an L-dwarf companion to the M1 dwarf CD-35 2722 A, discovered by the Gemini NICI planet-finding campaign [64]. Wahhaj et al. [64] report two epochs of relative astrometry and show that CD-35 2722 B is a bound companion on the basis of common proper motion. Results are shown in Table 4.10 and Figures 4.20 and 4.19.
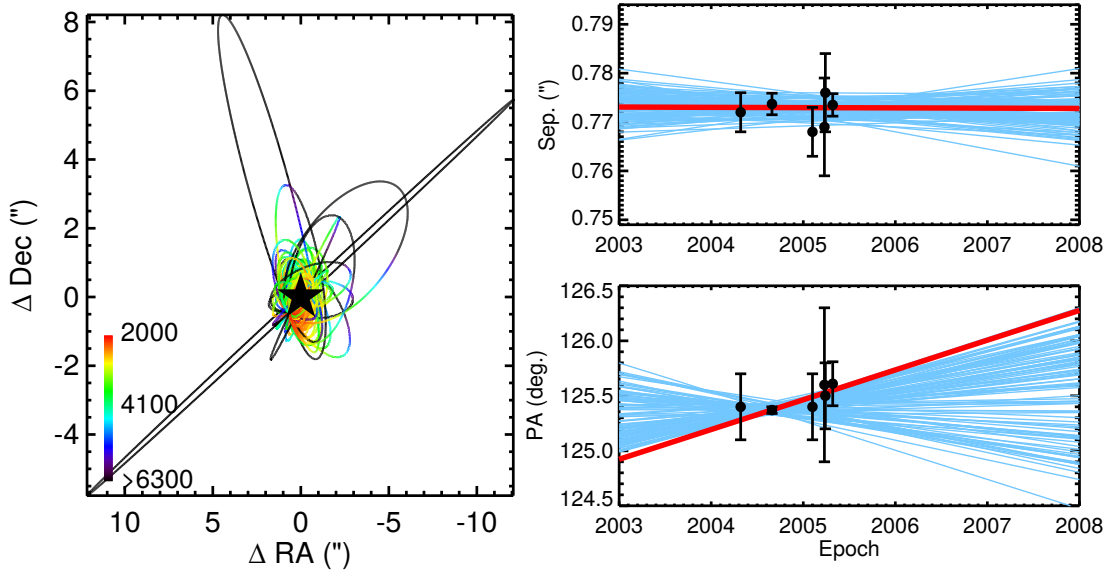
FIGURE 4.13: Depictions of 100 likely orbits fit to relative astrometry of 2M 1207 b with respect to 2M 1207 A. See Figure 4.2.

	unit	max probability	min χ^2	median	68% conf. range	95% conf. range
a	au	104.92	134.46	102	75-149	58-256
P	yr	1746.65	2337.20	1682	1054-2990	716-6723
e		0.1233	0.2839	0.32	0.09-0.59	0.01-0.74
i	°	123.6	115.6	127	119-144	112-165
ω	°	34.3	145.7	87	25-155	3-177
Ω	°	124.4	136.9	122	98-143	22-167
T_0	yr	3355.07	2028.69	3081.80	2534.01-4267.75	2068.56-7551.37

TABLE 4.9: Orbit of 2M 0103-55 (AB) b with respect to 2M 0103-55 (AB). Note: The acceptance rate was 0.32 %.

	unit	max probability	min χ^2	median	68% conf. range	95% conf. range
a	au	286.48	10048.78	115	74-216	53-520
P	yr	6858.18	1454272.75	1853	947-4772	580-17796
e		0.9058	0.9973	0.82	0.57-0.95	0.18-0.99
i	°	160.4	154.2	126	95-156	49-172
ω	°	110.4	136.7	128	32-163	3-177
Ω	°	72.1	98.2	75	58-104	20-158
T_0	yr	2088.36	2087.50	2125.23	2099.91-2184.95	2082.76-2531.59

TABLE 4.10: Orbit of CD-35 2722 B with respect to CD-35 2722 A. Note: The acceptance rate was 0.006 %.

With OFTI, we find a median semi-major axis of 115 au, with 68 % confidence between 74 and 216 au. The corresponding period is 1,853 years, with 68 % confidence between 947 and 4,772 years. Inclination angle and eccentricity remain mostly unconstrained. We use a uniform prior in eccentricity. The calculated orbital fraction for the orbit of CD-35 2722 B is $0.05 ^{+0.05}_{-0.03}$ %.
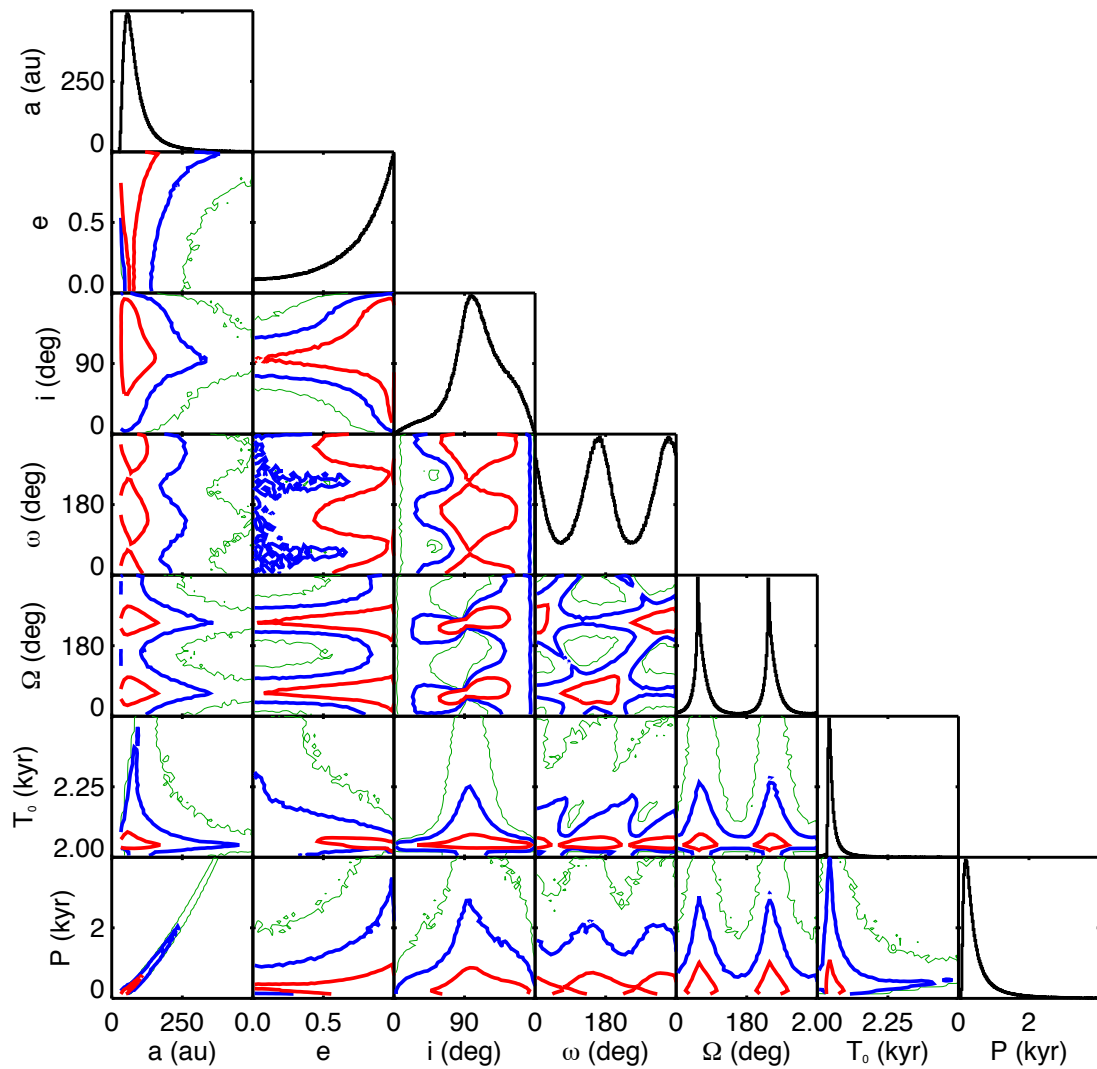
FIGURE 4.14: Triangle plots for the orbit of κ And B with respect to κ And A. See Figure 4.1.

4.2   Other OFTI Contributions to the Literature

In addition to results presented in Blunt et al [3], OFTI has contributed several orbit fits to the literature. In this section, I summarize those contributions, and outline some of the scientific conclusions these fits have enabled.

4.2.1   De Rosa et al 2015

51 Eri b [38] was the first exoplanet discovered by the Gemini Planet Imager Exoplanet Survey. From low-resolution spectra alone, young exoplanets are indistinguishable from older interloping brown dwarfs (objects that are not orbiting, but appear in the right
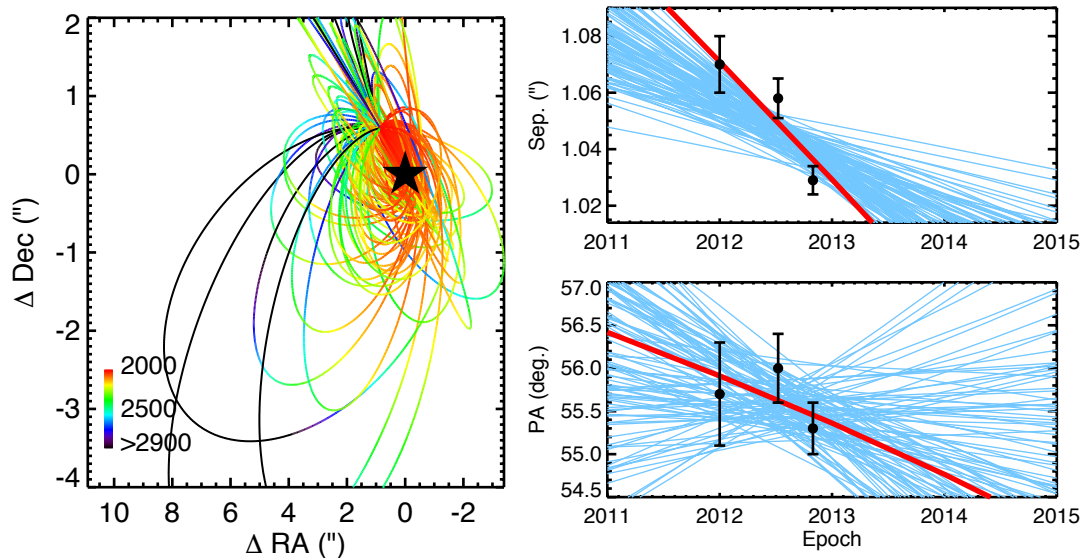
FIGURE 4.15: Depictions of 100 likely orbits fit to relative astrometry of κ And B with respect to κ And A. See Figure 4.2.

place at the right time to masquerade as an orbiting exoplanet). To support the argument that 51 Eri b was indeed an exoplanet, and not something else masquerading as one, De Rosa et al [14] amassed the following arguments:

- The spectrum of 51 Eri b did not appear consistent with that of a 1-10 kpc background object, such as a galaxy or a field star. Even so, De Rosa et al [14] calculated how such an object would move relative to 51 Eri over time, and compared this track with the range of trajectories possible for an orbiting exoplanet. The motion of the Earth around the Sun causes the sinusoidal background track seen in Figure 4.22, which was clearly inconsistent with the data. However, the motion was consistent with that of an orbiting exoplanet.

- To show how improbable it was for 51 Eri b to be an interloping brown dwarf, De Rosa et al [14] used an MCMC technique to determine parallax and distance posterior PDFs for 51 Eri b, assuming it to be an interloping brown dwarf. These PDFs, combined with knowledge about the field density of detectable brown dwarfs [38], was used to calculate the probability of 51 Eri b being an interloping brown dwarf: 2×10^{-7}.

Once the status of 51 Eri b as a confirmed exoplanet was firmly supported, we used OFTI to produce the first published orbital fits to 51 Eri b astrometry. Results are given in Figure 4.23, along with those of an implementation of MCMC. The inclination angle PDF was sufficiently constrained to allow us to compare the inclination angle of 51 Eri b with that of GJ 3305, a wide M-dwarf also orbiting 51 Eri. The inclination
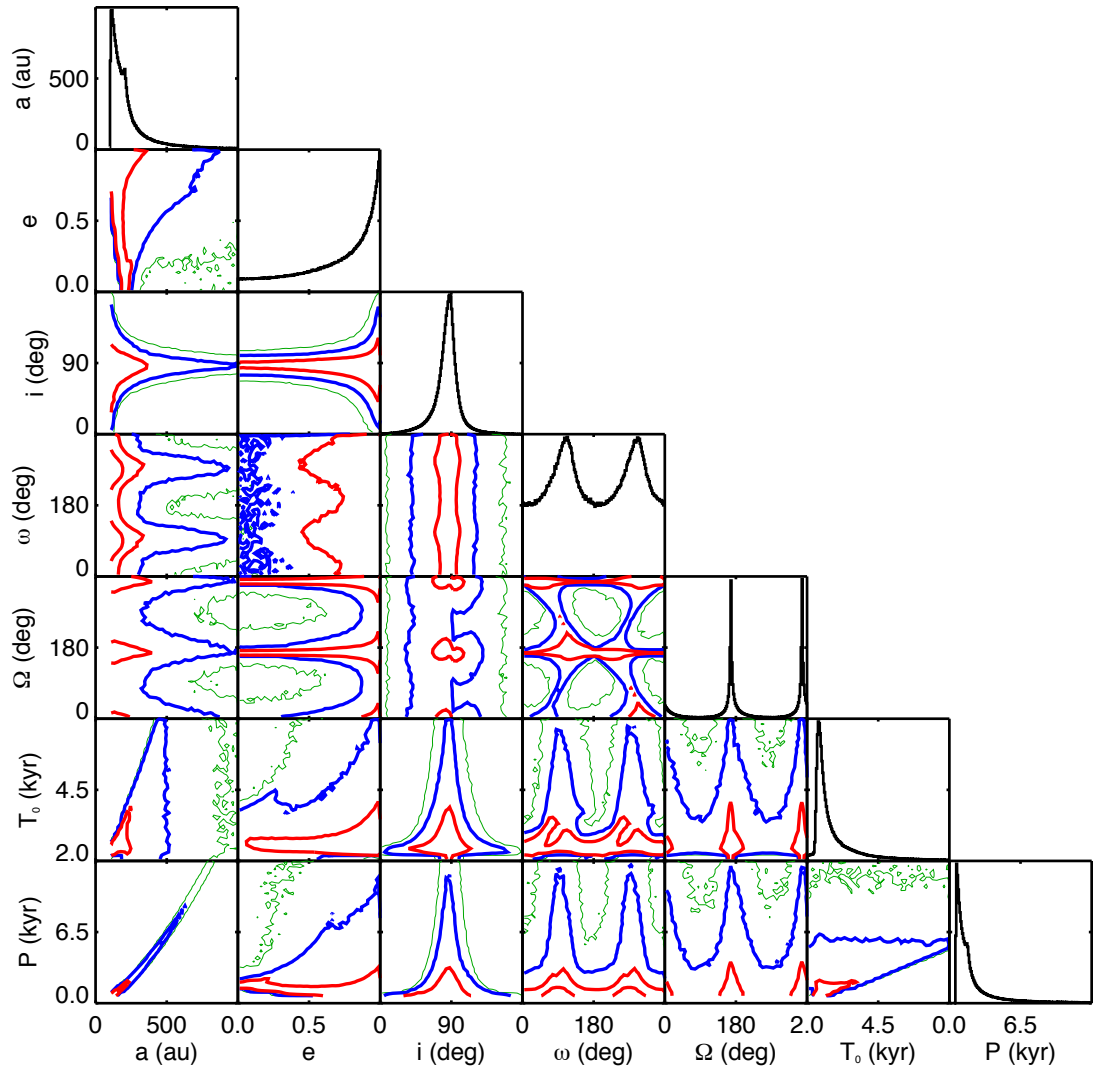
FIGURE 4.16: Triangle plots for the orbit of η Tel B with respect to η Tel A. See Figure 4.1.

angles of these two objects did **not** match, providing preliminary evidence that these objects did not form in the same way (i.e. in a protoplanetary disk).

4.2.2   Rameau et al 2016

Rameau et al. [54] present new constraints on the orbit of HD 95086 b, derived from astrometry taken with GPI between 2013 and 2016. HD 95086 hosts two radially separated protoplanetary disks, the outer of which has a well-characterized inclination angle: $i = 25 \pm 5°$ if the disk is orbiting in a counterclockwise direction, or $i = 155 \pm 5°$ if clockwise. Rameau et al [54] perform two OFTI fits: one using the standard exoplanet priors, and one with a restricted inclination prior corresponding to the inclination angle of the
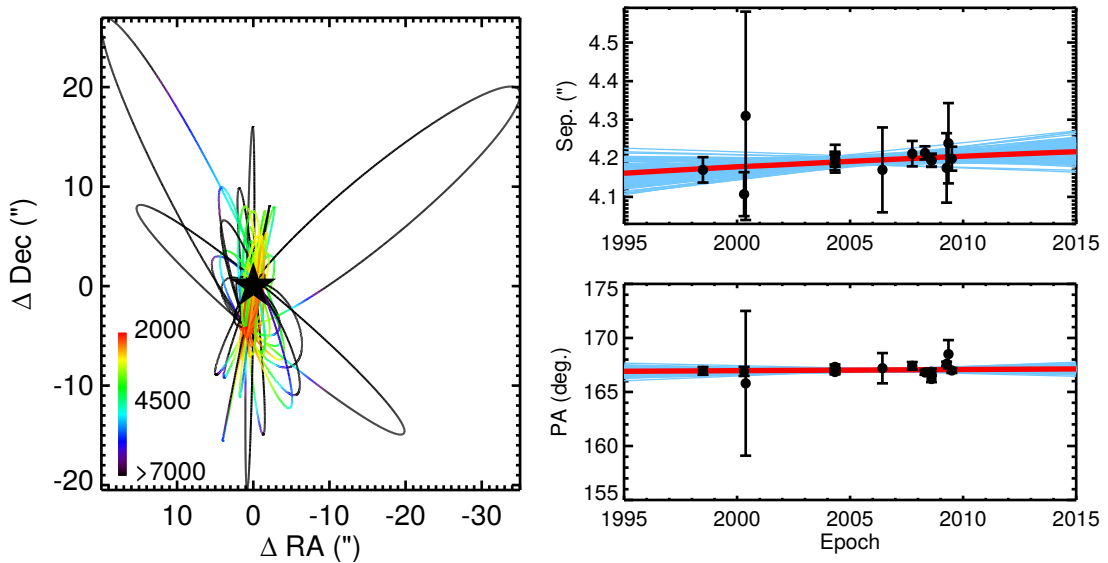
FIGURE 4.17: Depictions of 100 likely orbits fit to relative astrometry of η Tel B with respect to η Tel A. See Figure 4.2.

outer disk. Performing the latter orbit fit is equvalent to assuming that HD 95086 b and the outer disk are co-planar. Results are shown in Figure 4.24.

Regardless of the choice of inclination angle prior, our results indicate that HD 95086 b is unlikely to be responsible for carving out the inner disk, which is less than 10 au from HD 95086 (for example, under the assumption of co-planar exoplanet and outer disk, HD 95086 b is at periastron beyond 51 au with 68% confidence). See Figure 4.25 for a depiction of the range of possible orbits in the context of the system's disks. This problem is solved by assuming that additional exoplanets exist in the system, but are undetectable with GPI. Su et al [61] present three non-exhaustive additional planet scenarios based on n-body simulations of the HD 95086 system, which our OFTI fits allow us to analyze:

- Scenario B, in which planet b has an eccentricity of ~ 0.3 and another moderate-eccentricity planet exists at ~ 16 au, is neither confirmed nor eliminated by our results. Our fits favor low-eccentricity orbits for HD 95086 b, and the inner planet was not detectable from the observations outlined in [54].

- Scenario C, in which two additional low-eccentricity planets with equal masses (7 M_J each) exist at 12 au and 26 au, and planet b has an eccentricity of ~ 0.1 and a semi-major axis of ~ 56 au, was not supported by our analysis. The second planet would have been detected with 75% confidence, rendering this scenario unlikely.
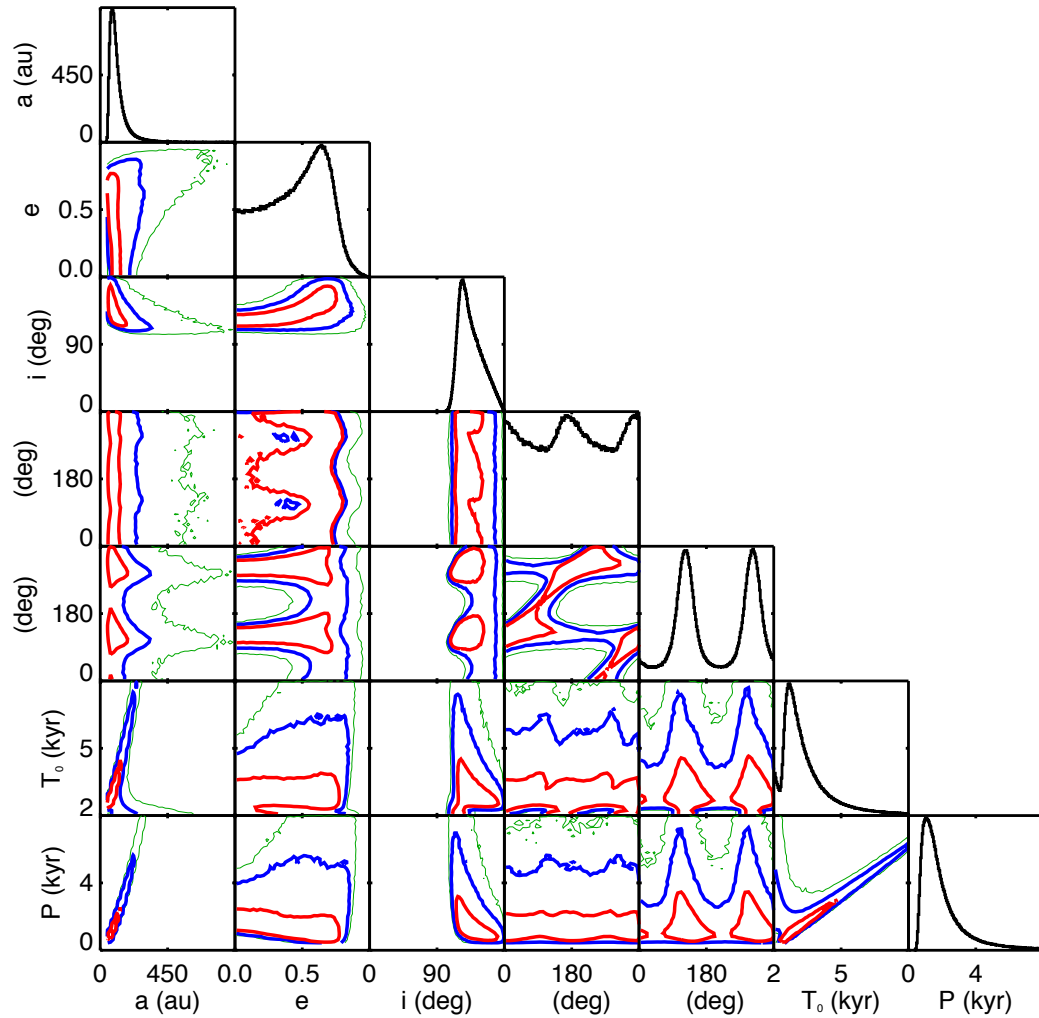
FIGURE 4.18: Triangle plots for the orbit of 2M 0103-55 (AB) b with respect to
2M 0103-55 (AB). See Figure 4.1.

- Scenario D, in which three additional 5 M_J planets exist in the gap between the
  inner and outer disks, was ruled out, as the hypothetical planet nearest to HD
  95086 b would have been detected with 100% confidence.

4.2.3 Bryan et al 2016

Bryan et al [6] present new astrometry on several planetary mass companions at wide
separations (> 50au) from their primaries. We performed OFTI fits to two such com-
panions that showed orbital motion: ROXs 12b and ROXs 42B b. These fits are shown
in Figures 4.26 and 4.27.

The orbit fits for both ROXs 12b and ROXs 42B b indicate a preference for low ec-
centricities, a result we showed to be independent of the choice of eccentricity prior.
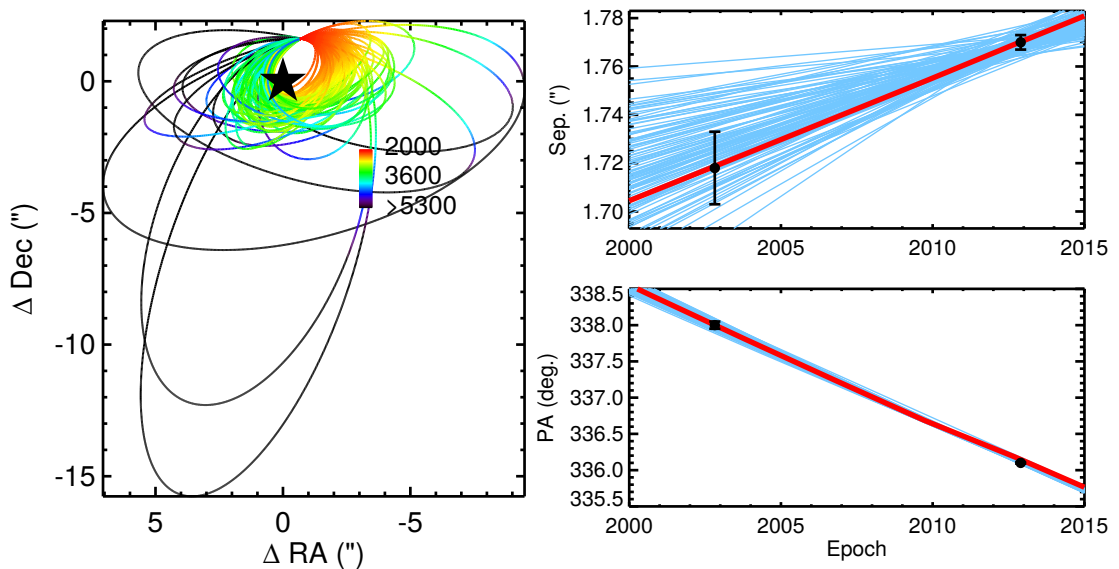
FIGURE 4.19: Depictions of 100 likely orbits fit to relative astrometry of 2M 0103-55 (AB) b with respect to 2M 0103-55 (AB). See Figure 4.2.

This result does not support the theory that these objects formed closer to their primary stars, then were scattered to their current locations by additional planets in their systems. Simulations show that giant scattered planets with wide separations typically have highly eccentric orbits, so these orbit fits point towards in-situ formation as a more probable scenario.

4.2.4   Johnson-Groh et al 2017

In Johnson-Groh et al [31], we perform the first orbit fit for HD 984 B, a low-mass brown dwarf companion to the young, nearby FV7 star HD 984. Using both archival astrometry and recent astrometry obtained with GPI, we determine that HD 984 B has $a = 18^{+10}_{-4}$au, corresponding to a median period of 70 years, $e = 0.18^{+0.29}_{-0.13}$, and $i = 119°\,^{+6}_{-5}$. These excellent constraints are shown in Figure 4.28.

4.2.5   Ngo et al 2017

As part of the study conducted by Ngo et al [45], Ngo et al examined the orbital architecture of six hierarchical triple stellar systems that host giant exoplanets. Each of these systems consists of:

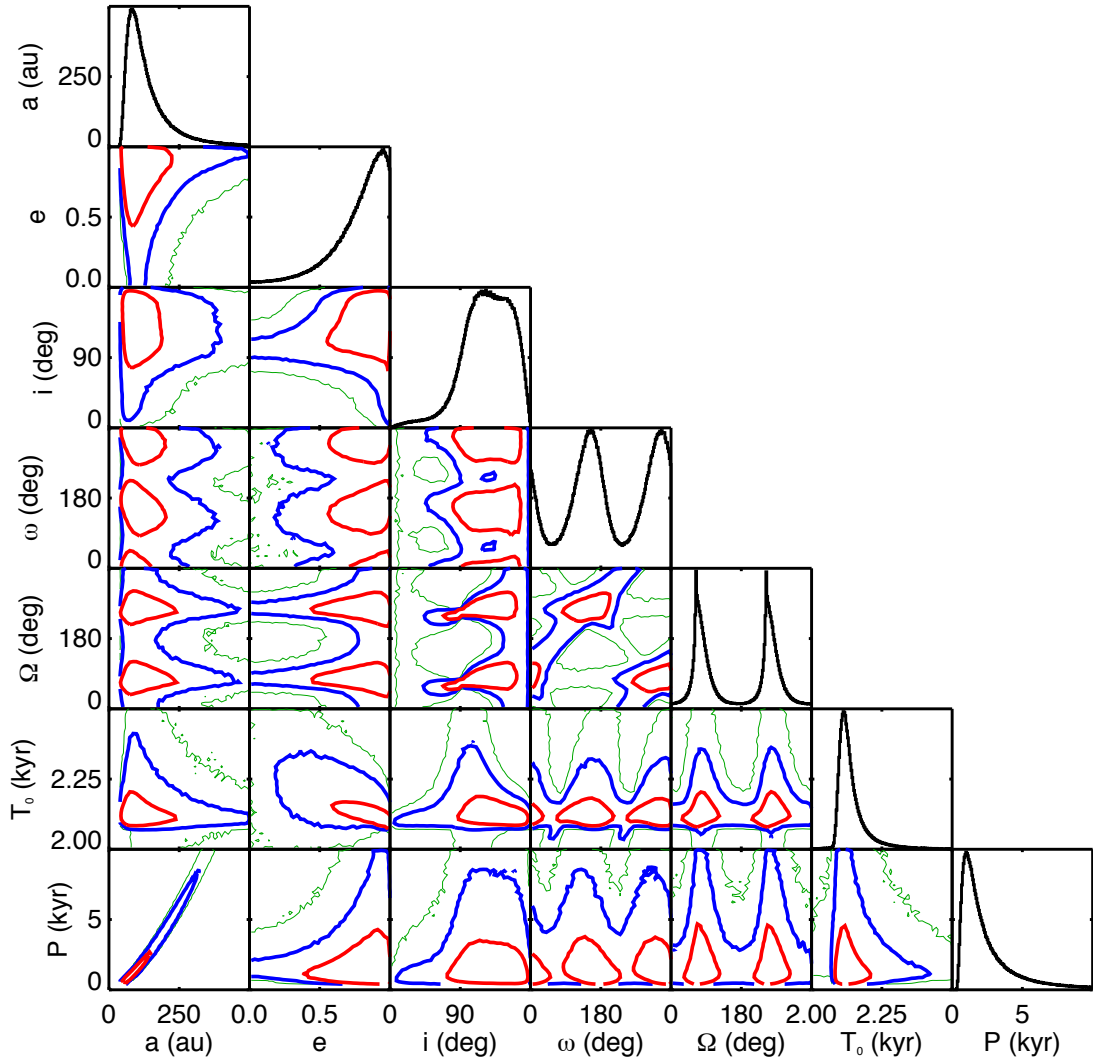- an A-component, with a closely orbiting exoplanet detectable with RV measurements.

FIGURE 4.20: Triangle plots for the orbit of CD-35 2722 B with respect to CD-35 2722 A. See Figure 4.1.

- a widely separated binary, called the B- and C-components. Both stars in the binary are much, much farther away from the A-component than the RV planet.

For each of these systems, Ngo et al were interested in the inclination angle of one star in the binary relative to the other star in the binary, i_{BC}, the inclination angle of the binary (treated as one object at its center of mass) relative to the A-component, i_{ABC}, and the inclination angle of the exoplanet relative to the A-component, i_b.

We first used OFTI to obtain posterior distributions of i_{BC} and i_{ABC} (and the corresponding posterior distributions of Ω, which are also needed to determine the orientation of the orbital plane) for each system. Ngo et al found that at the 2-σ level, one system has a binary orbital plane misaligned with the system orbital plane (the orbital plane of
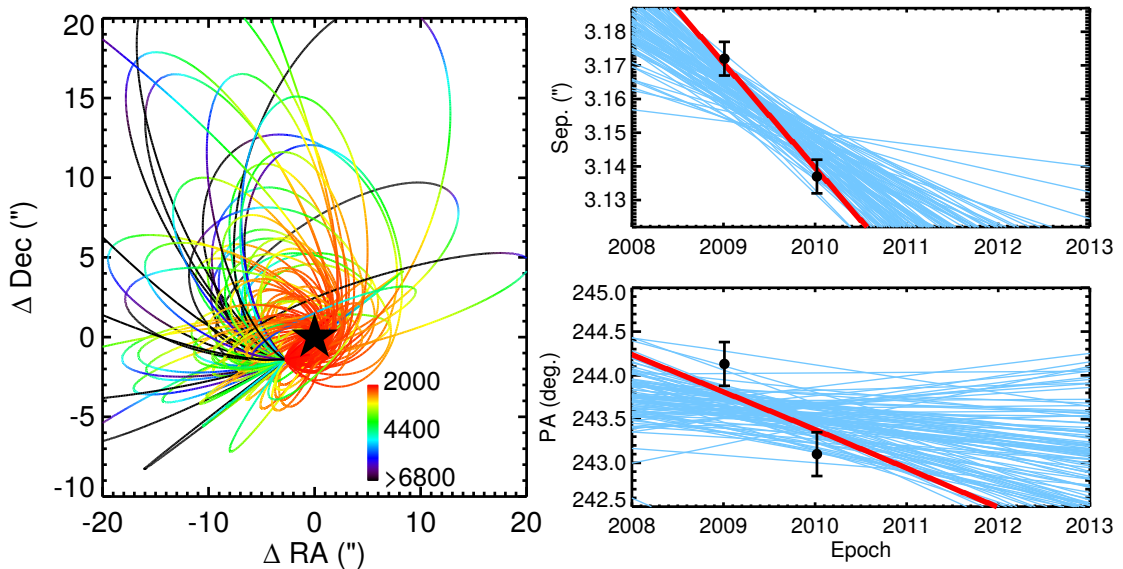
FIGURE 4.21: Depictions of 100 likely orbits fit to relative astrometry of CD-35 2722 B
with respect to CD-35 2722 A. See Figure 4.2.

the binary, treated as one object, with respect to the A-component), while the orbital
planes of two other systems are misaligned. The other three systems are neither aligned
nor misalinged at the 2-σ level.

Ngo et al next investigated i_b with respect to i_{BC} and i_{ABC}, where all i_b PDFs were
taken from the literature. i_b cannot be determined by RV measurements alone, so i_b de-
terminations exist only where the RV-exoplanet has also been detected using the transit
method. Three systems fit these criteria. Figure 4.29 shows the difference between the
i_b and i_{BC}, and the i_b and i_{ABC} PDFs. As the figure shows, the systems do not show
preference for inclination angle alignment or misalignment. Data from more systems is
needed to make definitive inferences about planetary formation in these systems, but
these results are an exciting first step in the analysis of such complex physical systems.

4.3   Modeling for Future Missions

OFTI's computational efficiency makes it an ideal tool for running large suites of or-
bital simulations, which are useful for setting requirements for the hardware of future
exoplanet imaging telescopes.

One such telescope, the *Wide Field Infrared Survey Telescope* (*WFIRST*), is a space tele-
scope with launch date tentatively scheduled for the mid-2020s. One of *WFIRST*'s main
science goals is discovering and characterizing exoplanets via direct imaging of reflected
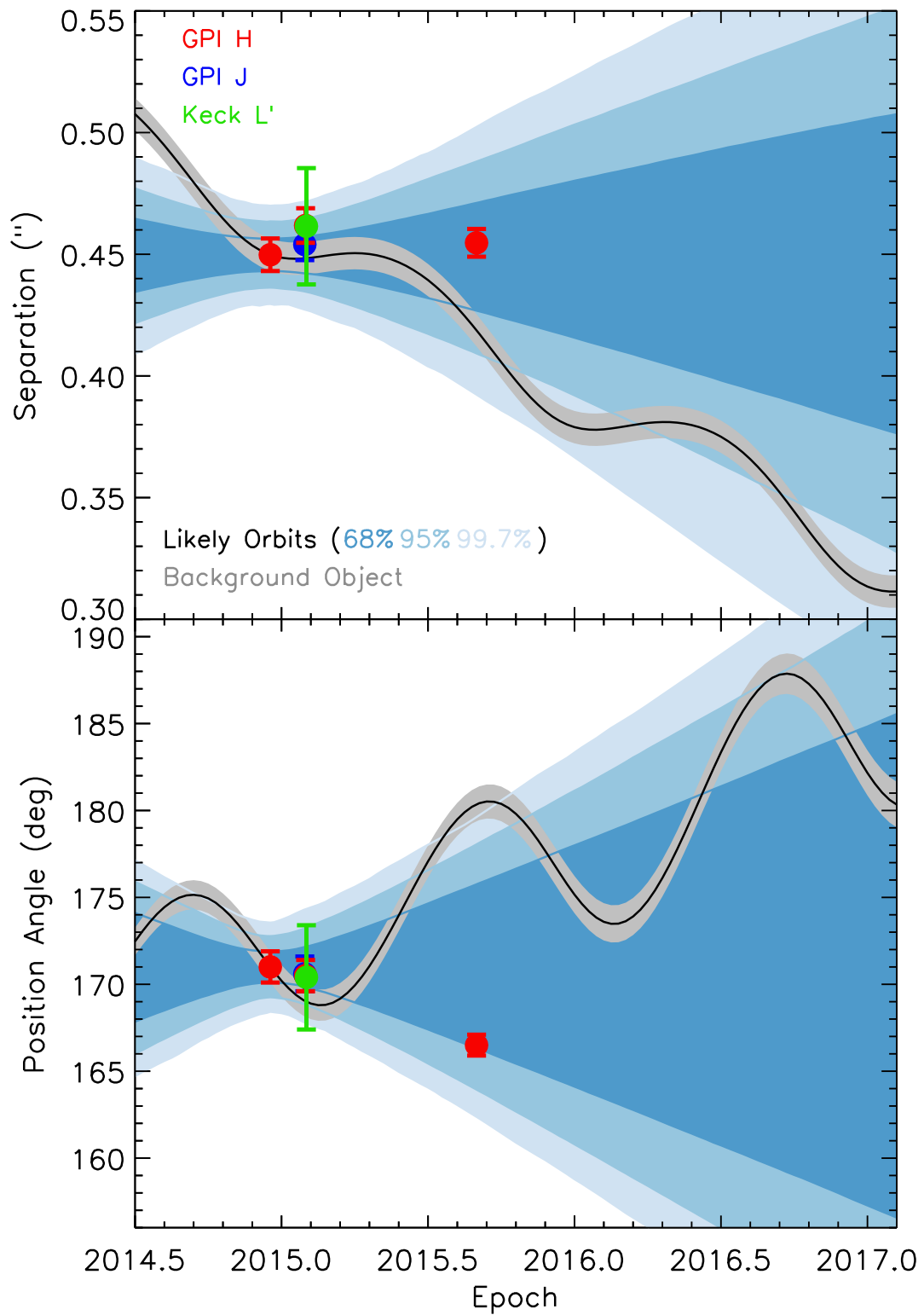starlight, and because of various technological improvements and other advantages (i.e.

FIGURE 4.22: Astrometry of 51 Eri b (red, green, and blue points), along with the predicted track for an infinitely distant background object and the possible tracks for an orbiting exoplanet, as calculated using the first four astrometric points. The September astrometry point lies many standard deviations away from the background location, but firmly inside the range of possible bound object trajectories.
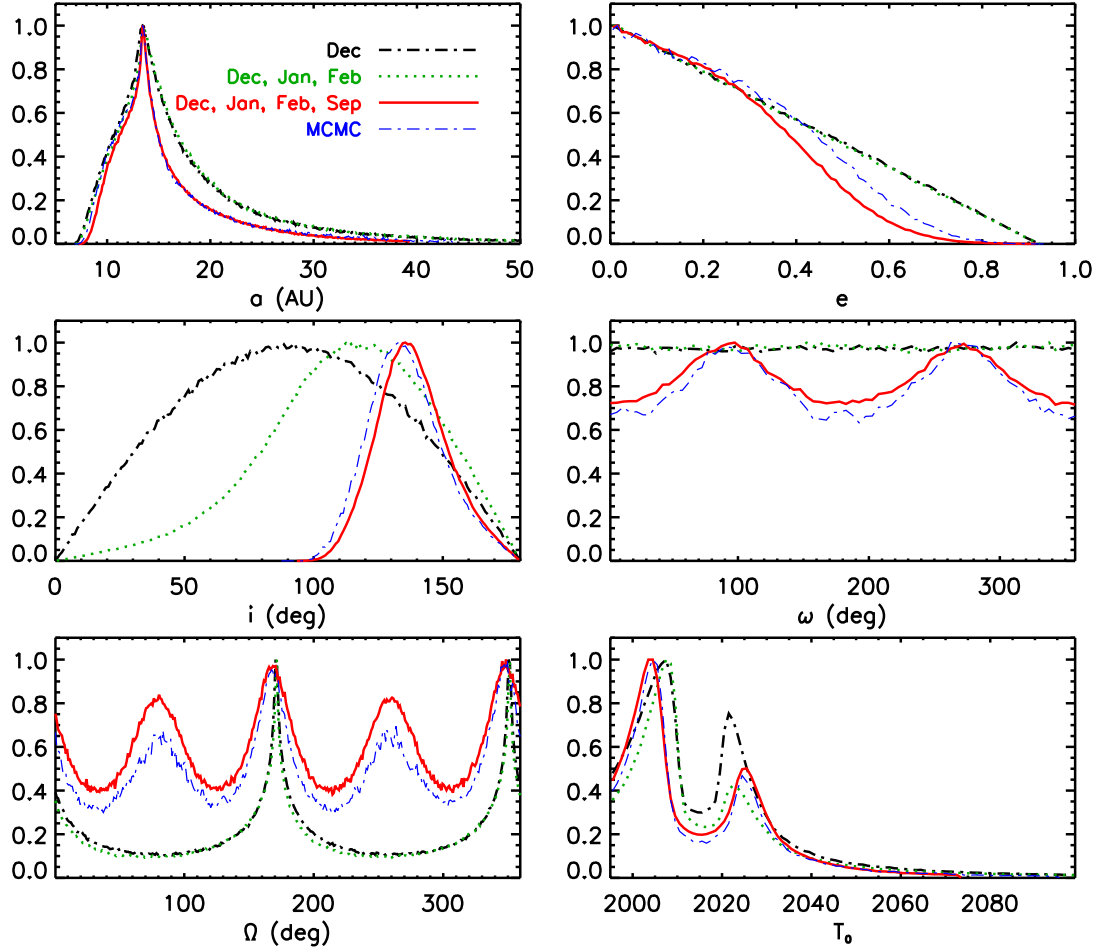
FIGURE 4.23: Orbital parameters of 51 Eri b, as fit to one, three, and four astrometric points by OFTI, and four astrometric points by MCMC. As expected, the posteriors change as the data covers a greater fraction of the orbit, and the inclination angle posterior becomes much more constrained. Since the publication of this paper, we found and corrected the bug in the OFTI code causing the slight disagreement between the OFTI and MCMC fits. As the figures earlier in this thesis show, our implementations of OFTI and MCMC now agree perfectly.

one of the first space telescopes with active wavefront control to reach contrasts better than 10^8), it will be able to detect exoplanets at much smaller projected separations and much higher contrasts. Therefore, over the *WFIRST* mission lifetime (approximately 6 years), we will see significant orbital motion in these planets, and can characterize their orbital parameters excellently.

Time in space is an extremely limited resource, however, so intelligent scheduling of follow-up observations is essential to maximize the amount of information obtainable with *WFIRST*. In order to devise a proper observing strategy, I my advisers and I are currently running suites of OFTI simulations for the *WFIRST* team. An example of the results of one of these simulations is shown in Figure 4.30. For this simulation, we pretended that *WFIRST* had just discovered the known RV-exoplanet 47 Uma c. We
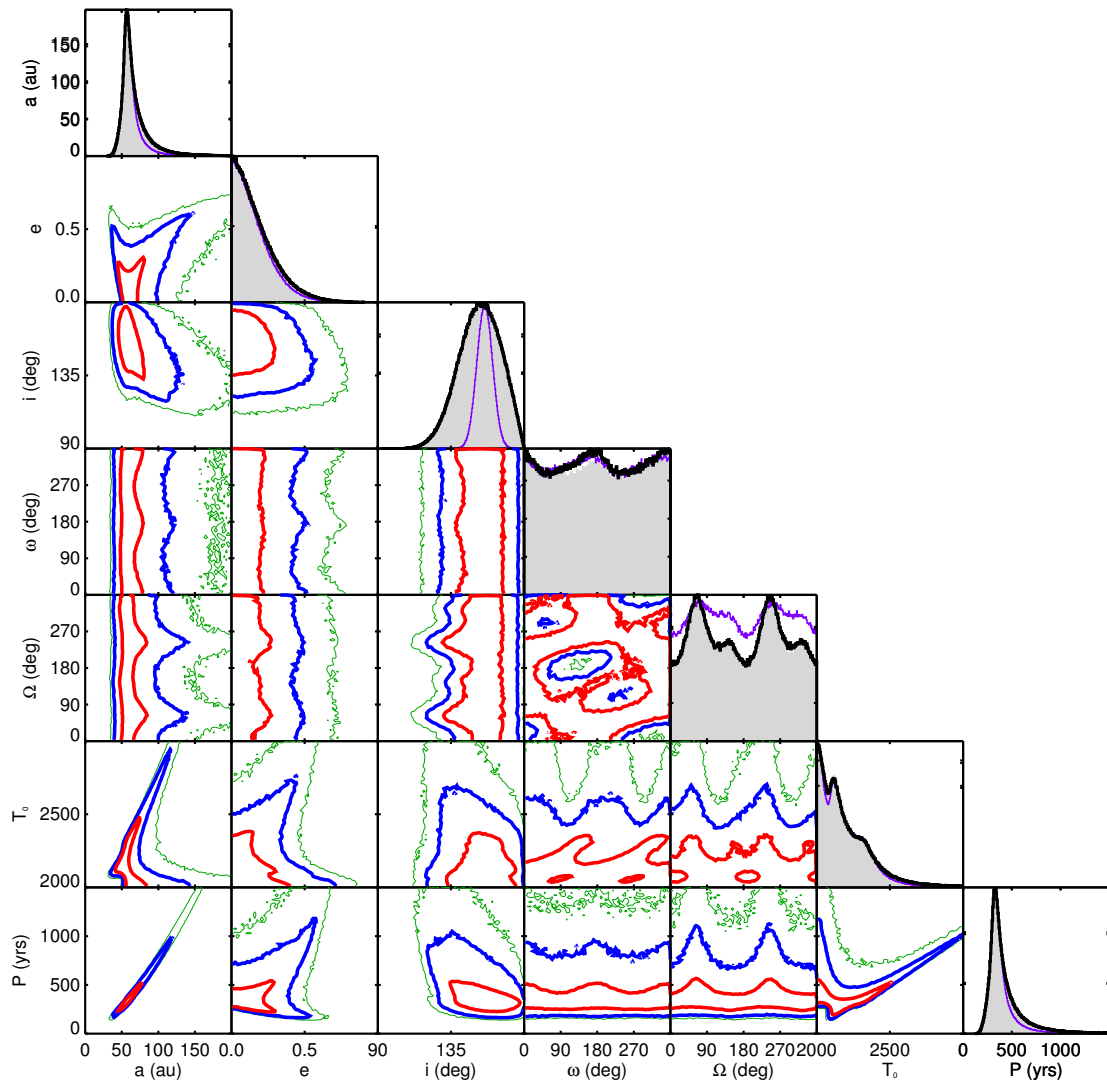
FIGURE 4.24: Triangle plot showing the orbit of HD 95086 b as inferred from astrometry taken before 2016. See Figure 4.1. Black lines in the diagonal cells show the OFTI fit performed using standard exoplanet priors, while gray shaded histograms show the same fit performed by an implementation of MCMC. The agreement between MCMC and OFTI is excellent. Purple lines show the OFTI fit performed using the restricted inclination angle prior. The results are mostly independent of our choice of prior; the largest change is the narrowing of the inclination angle posterior when the restricted inclination angle prior is used.
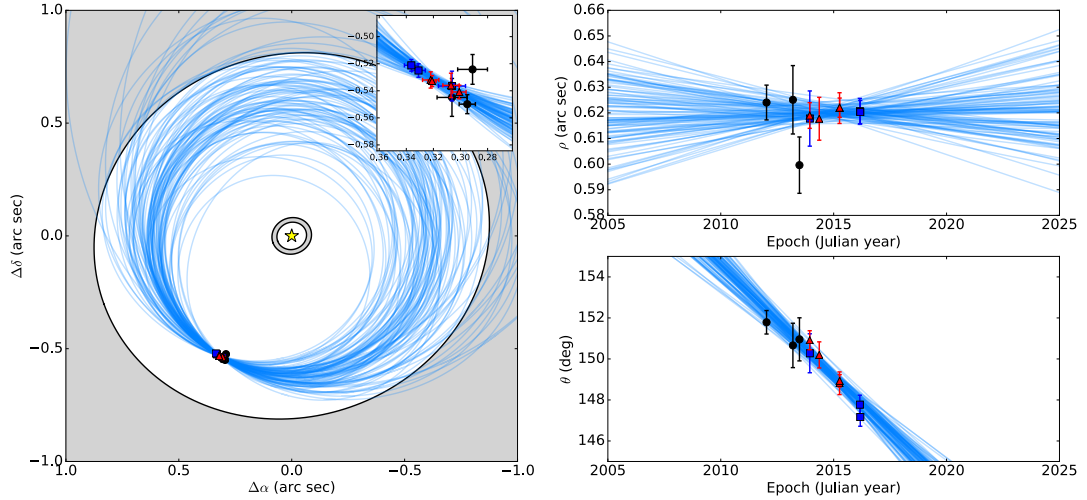
FIGURE 4.25: Depictions of 100 likely orbits fit to relative astrometry of HD 95086 b with respect to HD 95086 A. See Figure 4.2. The shaded gray regions show the locations of the inner and outer disks in the sky plane.

assigned the planet an inclination angle, since inclination angle is indeterminable by radial velocity measurements, and simulated astrometric points that *WFIRST* would measure. We did this three different times, for three different possible *WFIRST* observing cadences: taking a new astrometric point once every two years after discovery, once every year and four months, and once every year. We then iteratively ran OFTI on subsets of astrometry for each observing cadence, and plotted how the median, 1-σ, and 2-σ measurements of semi-major axis change with number of astrometric points available for each observing cadence. From these results, we can infer that for each observing cadence, typically four well-timed observations astrometric points are needed, and that once per year is the most efficient observing cadence for reducing orbital uncertainty.

We can perform the same analysis, varying the astrometric accuracy of *WFIRST* instead of the observing cadence, in order to help the *WFIRST* team set requirements for the telescope design.

The rate of reduction of orbital parameter uncertainty is also affected by the orbital phase at the time of observation. In Figure 4.31, we plot the standard deviations of inclination angle posteriors calculated for a known exoplanet, assumed to have been detected using radial velocity prior to *WFIRST* but imaged for the first time with *WFIRST*. We calculate the inclination angle posterior standard deviation for five different true values of the planet's inclination, and for several different initial *WFIRST* measurement epochs. As the figure shows, imaging this planet for the first time in the year 2026 rather than in 2027 results in an approximately 20° smaller inclination angle error on inclination angle.
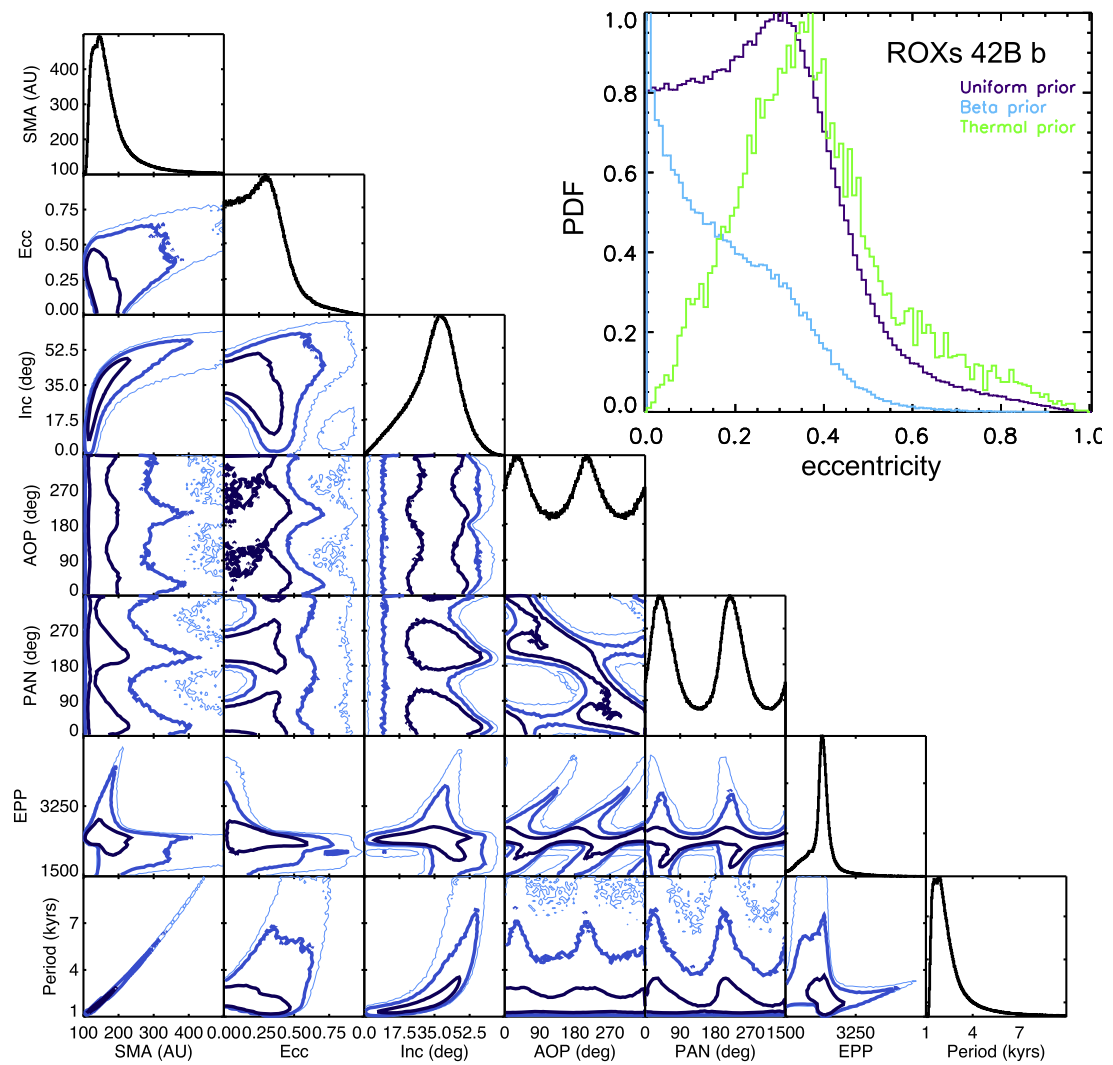
FIGURE 4.26: Triangle plot showing the orbit of ROXs 42B b. See Figure 4.1. To show that the preference for low eccentricities is independent of the choice of prior, we ran OFTI using several eccentricity priors. The results are shown in the top right panel.
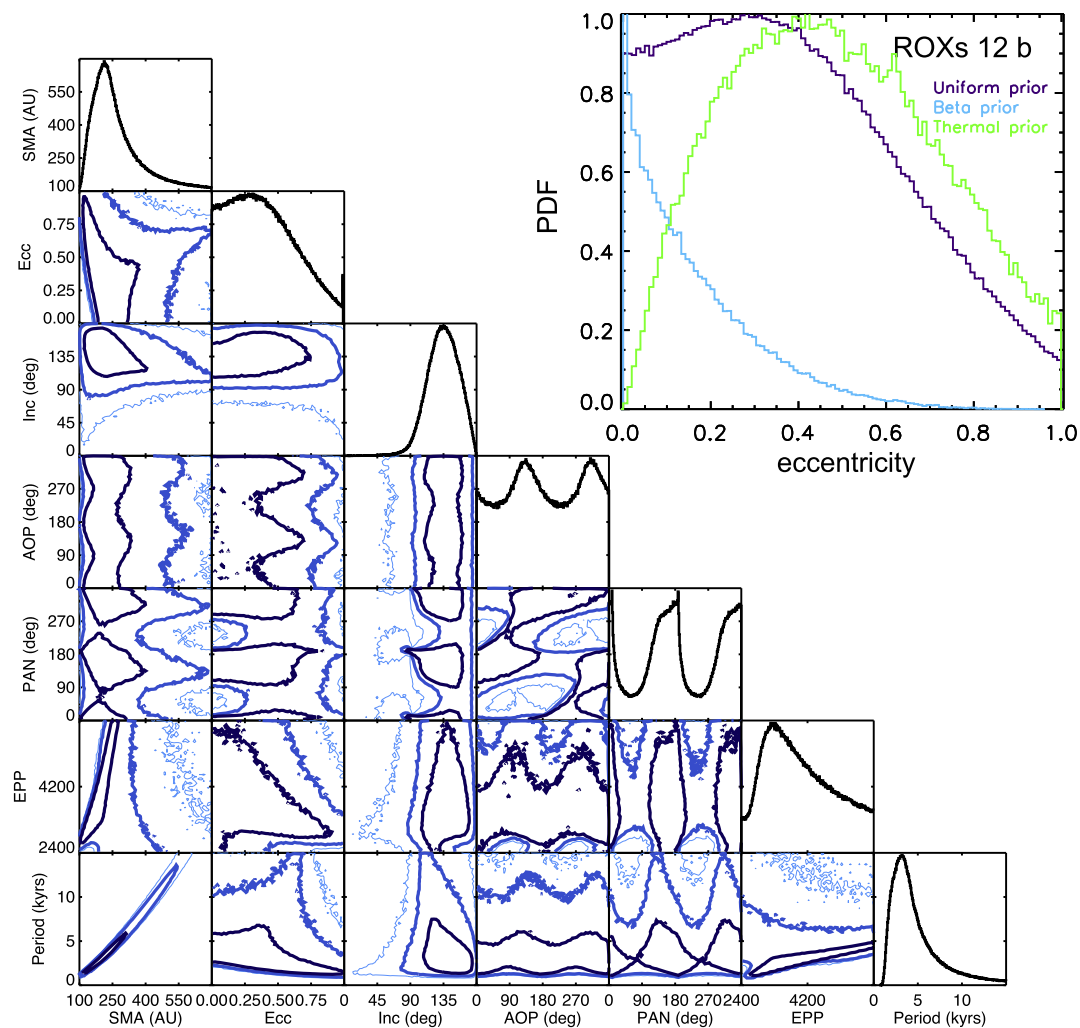
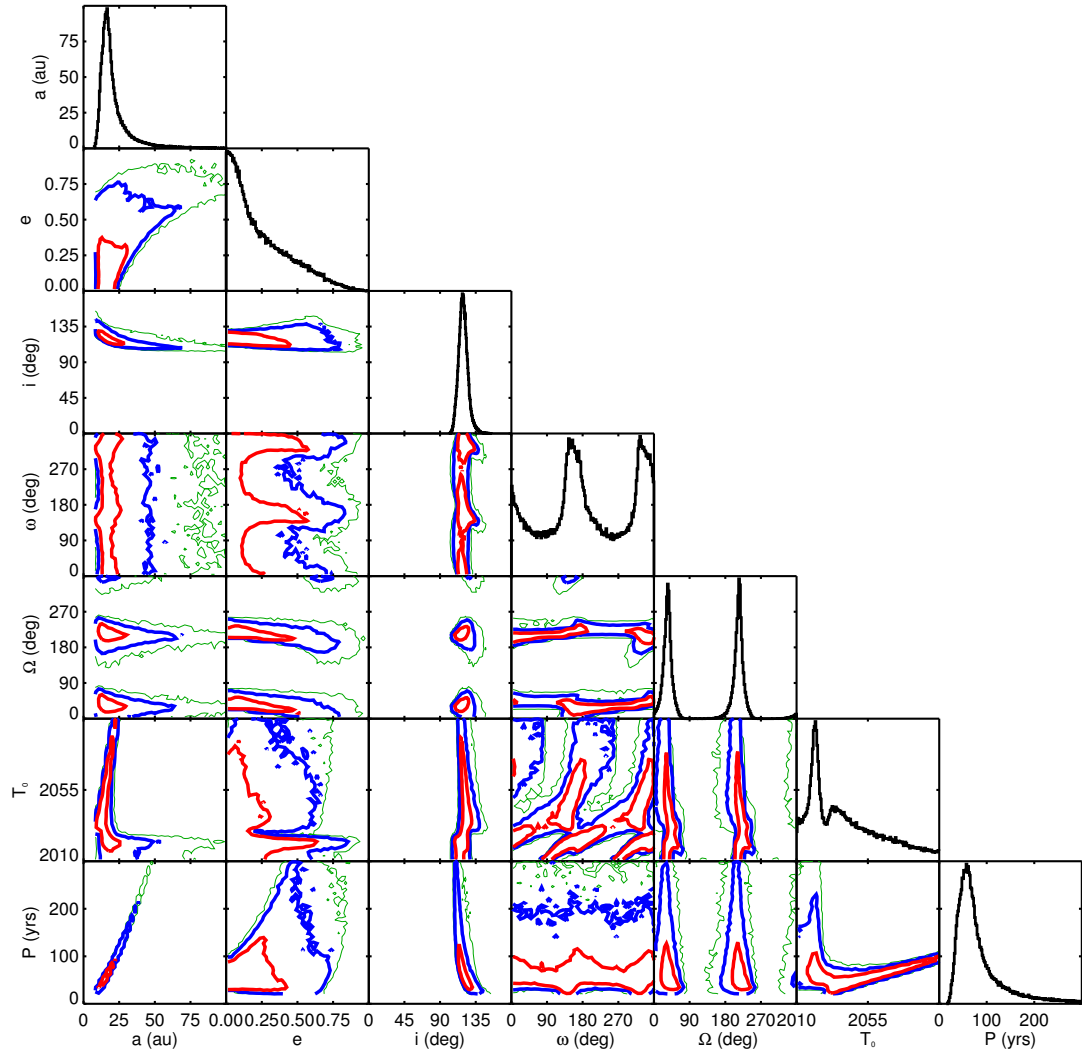FIGURE 4.27: Triangle plot showing the orbit of ROXs 12 b. See Figures 4.1 and 4.26.

FIGURE 4.28: Triangle plot showing the orbit of HD 984 B. See Figure 4.1. Note the excellent constraints on inclination angle and semi-major axis.
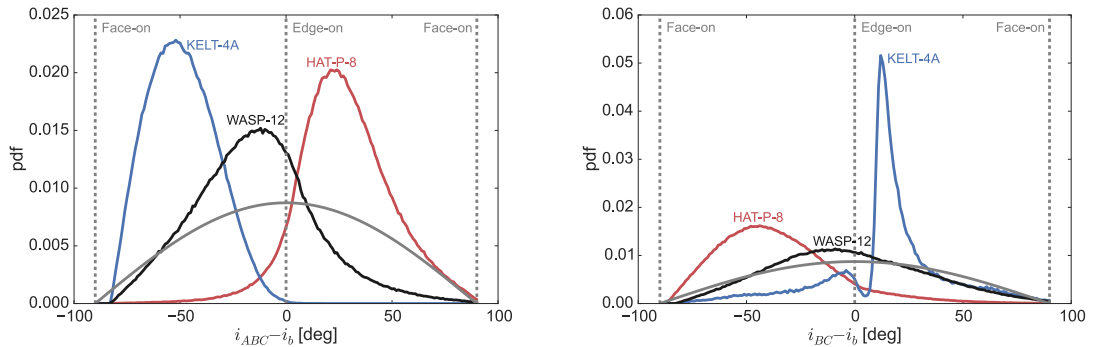

FIGURE 4.29: Left: differences between i_{ABC} and i_b for the three hierarchical triple systems that host transiting exoplanets also detectable by RV. The grey line shows the prior on Δi for an edge-on exoplanet. Right: differences between i_{BC} and i_b for the same three systems. No preference for inclination angle alignment or misalignment is clear from these results.
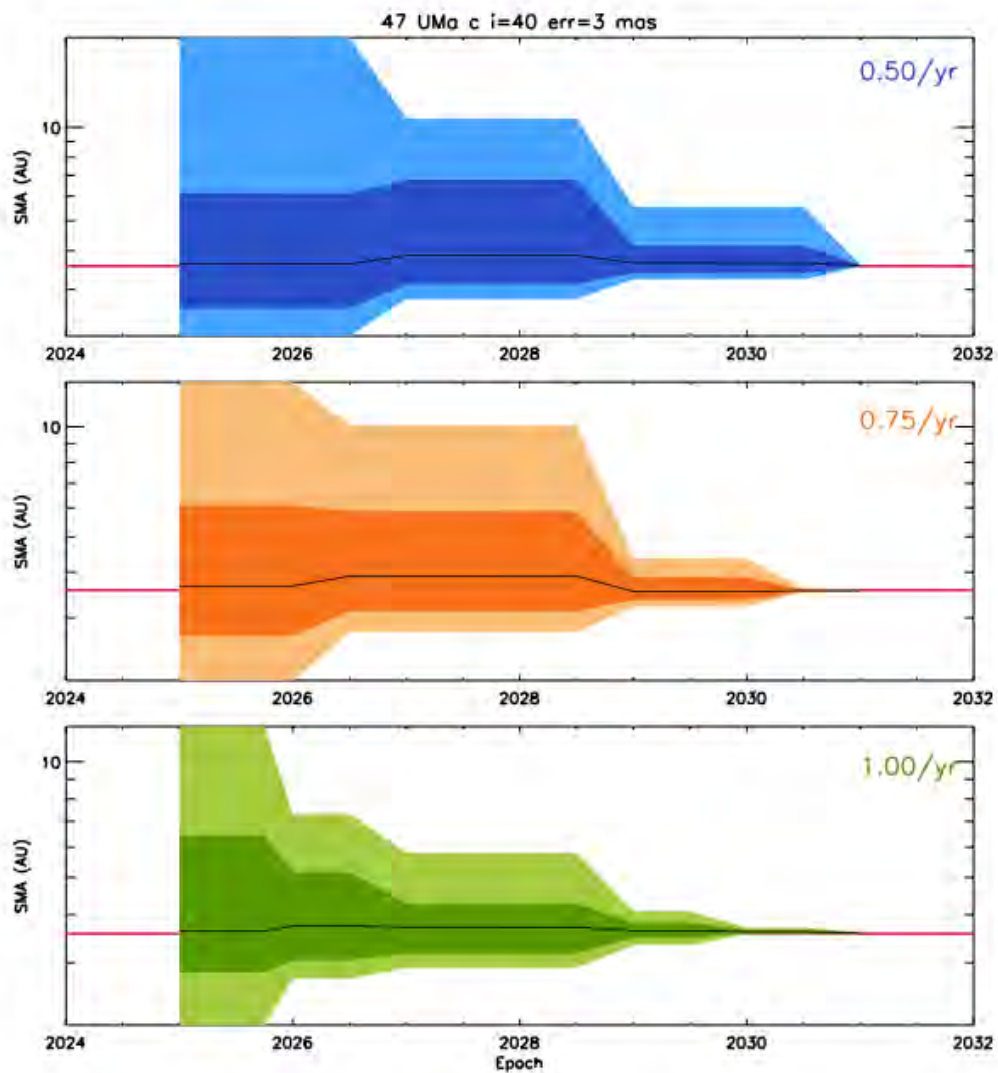
FIGURE 4.30: Reduction in semi-major axis uncertainty as a function of elapsed time for 47 Uma c, assumed to be discovered for the first time by *WFIRST*. Each panel shows the reduction of uncertainty for a particular observing cadence (printed in the top right corner of each panel). The red lines in each panel show the true a value, and the black lines show the median value of the a posterior as calculated using all available astrometry up to that time. The dark colors show the corresponding 1-σ values, and the light colors the 2-σ values.
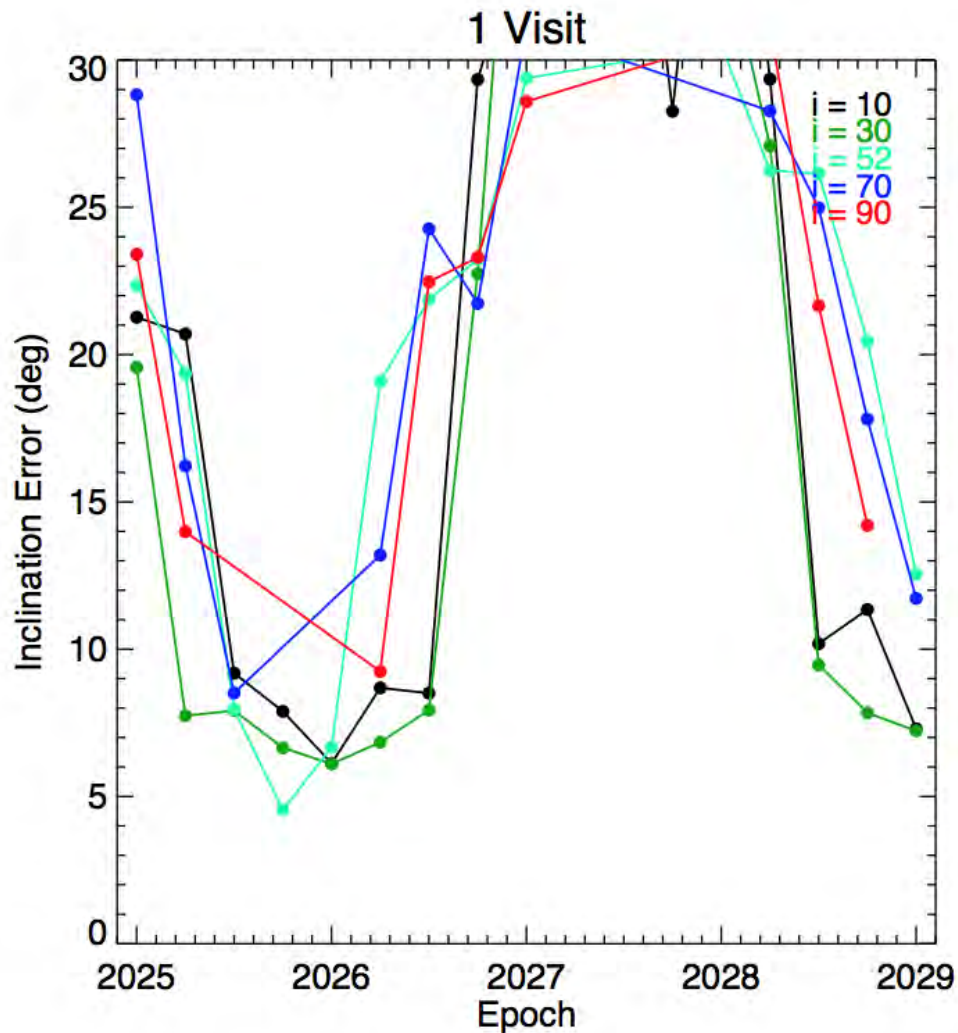
FIGURE 4.31: Standard deviations of simulated inclination angle posteriors, calculated for an exoplanet assumed to have been detected using radial velocity prior to *WFIRST* but imaged for the first time with *WFIRST*. The standard deviation is calculated as a function of actual inclination angle value (colors indicated in top right corner), and initial measurement epoch. Colored points indicate epochs where the planet is observable (i.e. it is not inside of the *WFIRST*'s inner working angle). This plot indicates that the most effective initial measurement epoch for reducing this planet's orbital uncertainty is approximately 2026.3 (assuming a *WFIRST* launch date of 2025). Even though the minimum inclination angle error occurs around 2025.9, several of the possible orbits would render the planet non-observable at 2025.9, so 2026.3 is the most intelligent choice.

Chapter 5

Conclusions & Future Directions

5.1 Conclusions

OFTI is a novel orbit-fitting method that reproduces the outputs of MCMC in orders of magnitude less time when fitting astrometric data covering only small fractions of orbits. A key difference from MCMC is that each OFTI orbit is independent of the others, whereas an MCMC chain produces a series of correlated values which only define the posterior PDF once the chains have fully converged. This difference makes OFTI an ideal tool when parameter estimates are required quickly, as in the context of a space mission. For example, when planning future observations, OFTI can quickly compute the expected decrease in errors on orbital parameters for different observing cadences without having to wait for multiple MCMC chains to converge.

In this thesis, I have demonstrated the accuracy of the OFTI method by comparing the outputs of our implementation of OFTI with those of MCMC, the speed of OFTI by analyzing the outputs produced for varying input orbital fraction, and the utility of OFTI by summarizing OFTI contributions to the literature.

OFTI is a useful tool for constraining the orbital parameters of directly imaged long-period exoplanets, brown dwarfs, and long-period stellar binaries. It has been applied to fitting the orbits of exoplanets imaged by the GPIES campaign and extremely long-period brown dwarfs, and will be used to fit the orbits of future *WFIRST* targets. OFTI's efficiency will be critical for a space-based mission like *WFIRST*, allowing future observations to be planned effectively and efficiently.

5.2 Future Directions

In the future, we plan to use OFTI to fit the orbits of giant exoplanets, brown dwarfs, binary stars, binary asteroids, stars orbiting the galactic center, and stars orbiting in the potential wells of nearby dwarf galaxies. We also plan to continue performing orbital simulations to aid in the hardware and mission designs of future exoplanet imaging space telescopes (see Section 4.3), such as WFIRST and HabEx. Finally, we would like to use OFTI to fit the orbits of a statistically significant number of long-period brown dwarfs in order to determine the underlying brown dwarf eccentricity distribution.

We would also like to expand the capability of the OFTI algorithm. One idea involves minimizing astrometric biases incurred by instrument calibration errors by introducing additional true north and plate scale parameters to the fit for each instrument contributing data to a set of astrometry. In addition, we have begun to explore methods of modifying OFTI to fit combined imaging and radial velocity data sets, which will become increasingly common as imaging technology improves over the next few decades.

Bibliography

[1] Batalha 2014, PNAS, 111, 35

[2] Beust, H., Augereau, J.-C., Bonsor, A. et al. 2014, A&A, 561, A43

[3] Blunt, S., Nielsen, E. L., De Rosa, R. J., et al. 2017, AJ, 153, 229

[4] Bonnefoy, M., Currie, T., Marleau, G.-D., et al. 2014, A&A, 562, A111

[5] Bowler, B. P. 2016, PASP, 128, 968

[6] Bryan, M. L., Bowler, B. P., Kuntson, H. A., et al. 2016, ApJ, 827, 100

[7] Carson, J., Thalmann, C., Janson, M., et al. 2013, ApJL, 763, L32

[8] Chauvin, G., Lagrange, A. M., Dumas, C., et al. 2004, A&A, 435, L29

[9] Chauvin, G., Lagrange, A.-M., Dumas, C., et al. 2005, A&A, 438, 2

[10] Chauvin, G., Lagrange, A.-M., Beust, H., et al. 2012, A&A, 542, A41

[11] Claudi, R., Gratton, R., Desidera, S., et al. 2016, Mem SAIt, 87, 132

[12] Currie, T., Daemgen, S., Debes, J., et al. 2014, ApJL, 780, 30

[13] Delorme, P., Gagné, J, Girard, J. H., et al. 2013, A&A, 553, L5

[14] De Rosa, R., Nielsen, E. L., Blunt, S. C., et al. 2015, ApJL, 814, L3

[15] Duchêne, G., & Kraus, A. 2013, ARAA, 51, 269

[16] Dupuy, T J., Liu, M. C., Leggett, S. K., et al. 2015, ApJ, 805, 56

[17] Dupuy, T. J., Kratter, K. M., Kraus, A. L., et al. 2016, ApJ, 817, 80

[18] Fabrycky, D. C. & Murray-Clay, R. A. 2010, ApJ, 710, 1408

[19] Fekel, F. C., Jr. 1981, ApJ, 246, 879

[20] Ford, E. B. 2004, AIP Conference Proceedings, 713, 27

[21] Ford, E. B. 2006, 2006, ApJ, 642, 505

[22] Foreman-Mackey, D., Hogg, D. W., Lang, D., et al. 2013, PASP, 125, 306

[23] Garcia, E. V., Currie, T., Guyon, O., et al. 2016, ApJ, 834, 162

[24] Geissler, K., Chauvin, G., & Sterzik, M. F. 2008, A&A, 480, 193

[25] Gelman, A., & Rubin, D. B. 1992, Statist. Sci., 7, 457

[26] Ghez, A. M., Salim, S., Weinberg, N. N., et al. 2008, ApJ, 689, 1044

[27] Guenther, E. W., Neuhäuser, R., Huélamo, N., et al. 2001, A&A, 365, 514

[28] Hinkley, S., Pueyo, L., Faherty, J. K. 2013, ApJ, 779, 153

[29] Huélamo, N., Nürnberger, D. E. A., Ivanov, V. D., et al. 2010, A&A, 521, L54

[30] Janson, M., Carson, J., Thalmann, C., et al. 2011, ApJ, 728, 85

[31] Johnson-Groh, M., Marois, C., De Rosa, R. J., et al. 2017, AJ, 153, 190

[32] Kraus, A. L., Ireland, M. J., Cieza, L. A., et al. 2014, ApJ, 781, 20

[33] Konopacky, Q. M., Marois, C., Macintosh, B. A., et al. 2016, ApJ, 152, 28

[34] Kuzuhara, M., Tamura, M., Kudom T., et al. 2013, ApJ, 774, 1

[35] Lagrange, A.-M., De Bondt, K., Meunier, N., et al. 2012, A&A, 542, A18

[36] Lowrance, P. J., Schneider, G., Kirkpatrick, J. D., et al. 2000, ApJ, 541, 390

[37] Macintosh, B., Graham, J., Ingraham, P., et al. 2014, PNAS, 111, 35

[38] Macintosh, B., Graham, J. R., Barman, T., et al. 2015, Science, 350, 64

[39] Maire, A.-L., Bonnefoy, M., Ginski, C., et al. 2016, A&A, 587, A56

[40] Mawet, D., David, T., Bottom, M., et al. 2015, ApJ, 811, 103

[41] Mesa, D., Vigan, A., D'Orazi, V., et al. 2016, A&A, 593, A119

[42] Millar-Blanchaer, M. A., Craham, J. R., Pueyo, L. P., et al. 2015, ApJ, 811, 1

[43] Mohanty, S., Jayawardhana, R., Huélamo, N., et al. 2007, ApJ, 657, 1064

[44] Neuhäuser, R., Ginski, S., Schmidt, T. O. B., et al. 2011, MNRAS, 416, 1430

[45] Ngo, H., Knutson, H. A., Bryan, M. L., et al 2017, AJ, eprint arXiv:1704.02326

[46] Nielsen, E. L. & Close, L. M. 2010, ApJ, 717, 878

[47] Nielsen, E. L., Liu, M. C., Wahhaj, Z., et al. 2012, ApJ, 750, 53

[48] Nielsen, E. L., Liu, M. C., Wahhaj, Z., et al. 2013, ApJ, 776, 4

[49] Nielsen, E. L., Liu, M. C., Wahhaj, Z., et al. 2014, ApJ, 794, 158

[50] Patience, J., King, R. R., De Rosa, R. J., et al. 2012, A&A, 540, A85

[51] Perrin, M. D., Maire, J., Ingraham, P., et al. 2014, SPIE, 9147, id. 91473J

[52] Press, W. H., Rybicki, G. B., & Hewitt, J. N. 1992, ApJ, 385, 416

[53] Price-Whelan, A. M., Hogg, D. W., Foreman-Mackey, D., et al. 2017, ApJ, 837, 20

[54] Rameau, J., Nielsen, E. L., De Rosa, R. J., et al. 2016, ApJL, 822, 2

[55] Sallum, S., Eisner, J. A., Close, L. M., et al. 2015, ApJ, 801, 85

[56] Savransky, D., & Garrett, D. 2015, J. Astron. Telesc. Instrum. Syst. 2(1), 011006

[57] Shkolnik, E. L., Anglada-Escudé, G., Liu, M. C., et al. 2012, ApJ, 758, 56

[58] Siess L., Dufour E., & Forestini M. 2000, A&A, 358, 593

[59] Song, I., Schneider, G., Zuckerman, B., et al. 2006, ApJ, 652, 724

[60] Spergel, D., Gehrels, N., Baltay, C., et al. 2015, eprint arXiv:1503.03757

[61] Su, K. Y. L., Rieke, G. H., Stapelfeldt, K. R., et al. 2009, ApJ, 705, 314

[62] Tokovinin, A. 2004, Revista Mexicana de Astronomía y Astrofísica (Serie de Conferencias), 21, 7

[63] Traub, W. A., Breckinridge, J., Greene, T. P., et al. 2016, JAST, 2, 011020

[64] Wahhaj, Z., Liu, M. C., Biller, B. A., et al. 2011, ApJ, 729, 139

[65] Wang, J. J., Graham, J. R., Pueyo, L. P., et al. 2016, AJ, 152, 97

[66] Wyatt, M. C., Smith, R., Su., K. Y. L., et al. 2007, ApJ, 663, 365

[67] Zurlo, A., Vigan, A., Galicher, A-L., et al. 2016, A&A, 587, A57